



Nuclear Instruments and Methods in Physics Research A

journal homepage: www.elsevier.com/locate/nima

Review

Hadron Calorimetry

Nural Akchurin*, Richard Wigmans

Texas Tech University, Department of Physics, Lubbock, TX 79409, USA

ARTICLE INFO

Available online 7 November 2011

Keywords:

Hadron calorimetry
Hadron cascades
Sampling calorimetry

ABSTRACT

Hadron calorimetry has been a rapidly developing field in the past few decades. Perhaps not too far in the future, a realistic calorimeter will be capable of measuring the energies of all the fundamental particles with $\sim 1\%$ precision. Currently, calorimeters with unprecedented complexity attest to the knowledge and experience that have been accumulated in high energy physics. In this review, we touch on fundamental concepts and explain new developments that we expect to be important in the future. In addition to describing applications in accelerator-based high energy physics, we briefly mention the use of hadron calorimeters in other fields.

© 2011 Elsevier B.V. All rights reserved.

Contents

1. Introduction	80
2. Hadronic shower development in dense matter	81
2.1. Differences with electromagnetic showers	81
2.2. Hadronic shower profiles	81
2.3. Characteristics of the em shower component	81
2.4. Effects of nuclear interactions	82
3. Effects of non-compensation	83
4. Calibration of calorimetry systems	83
4.1. Unsegmented calorimeters	84
4.2. Segmented calorimeters	84
4.3. Calibration and hadronic signal linearity	84
4.4. Electromagnetic showers in segmented calorimeters	85
5. Calorimeters at the LHC	86
5.1. ATLAS	86
5.2. CMS	86
6. Simulations	90
7. New developments in calorimetry	91
7.1. Particle flow analysis	91
7.2. Dual-readout calorimetry	92
7.3. Challenges	94
8. Non-accelerator applications of hadron calorimetry	94
9. Summary	96
References	96

1. Introduction

The term hadron calorimetry is strongly linked to experiments at particle accelerators, where detector systems typically contain

an electromagnetic (em) and a hadronic calorimeter section. Elsewhere, e.g., in cosmic-ray experiments, detectors based on total absorption of the entering particles (calorimeters) do not make this distinction. We would like to stress that the distinction between em and hadron calorimeters is largely artificial. In a typical experiment at the Large Hadron Collider (LHC) or its predecessors, high-energy hadrons deposit one to two thirds of their energy in the em section. Therefore, the properties of the em

* Corresponding author.

E-mail address: nural.akchurin@ttu.edu (N. Akchurin).

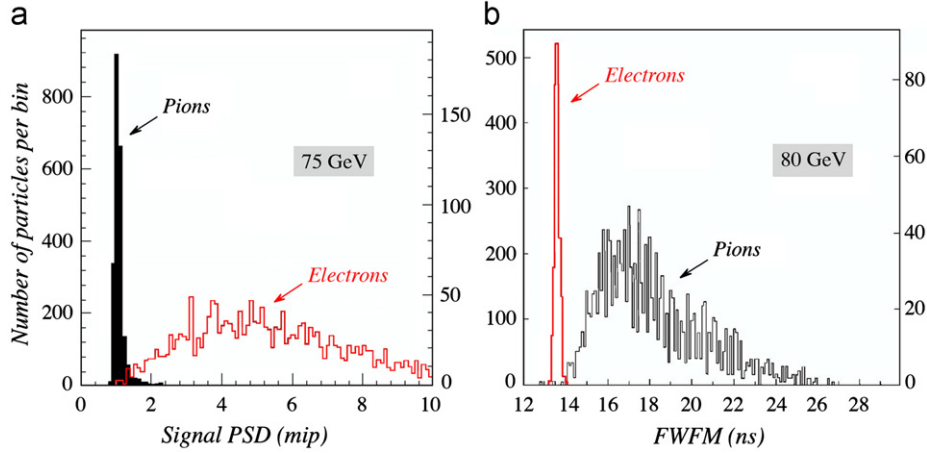


Fig. 1. Two different methods to distinguish electrons from pions in a calorimeter. Histograms in (a) show the signal distributions in a $2X_0$ thick preshower detector (PSD) [8]. In (b), the distributions of the duration of the pulse (defined as the full width at one-fifth of the maximum amplitude) are plotted [9]. In both figures, the left hand scale refers to the narrow distribution, the right hand scale to the broad one.

calorimeter section should be an integral part of any discussion about hadron calorimetry in these experiments. Stand-alone em calorimeters are discussed elsewhere in this volume [1].

Calorimetric techniques used to detect hadrons cover a very wide energy range, from thermal neutrons, which have kinetic energies of a small fraction of 1 eV, to the highest-energy particles observed in nature, which reach the Earth from outer space as cosmic rays carrying 10^{20} eV or more. In accelerator-based particle physics experiments, hadron calorimeters are typically used to detect protons, pions, kaons and fragmenting quarks and gluons (jets) with energies in the GeV–TeV range. In this review, we mainly discuss the latter instruments and focus on relatively recent developments. For a more extensive introduction to this field, the reader is referred to Refs. [2–6].

2. Hadronic shower development in dense matter

2.1. Differences with electromagnetic showers

The development of hadronic cascades in dense matter differs in essential ways from that of electromagnetic ones, with important consequences for calorimetry. Hadronic showers consist of two distinctly different components:

1. An *electromagnetic* component: π^0 s, η s and other mesons generated in the absorption process decay into γ s which develop em showers.
2. A *non-electromagnetic* component, which combines essentially everything else that takes place in the absorption process.

For the purpose of calorimetry, the main difference between these components is that some fraction of the energy contained in the non-em component does not contribute to the measured signals. This *invisible energy*, which mainly consists of the binding energy of nucleons released in the numerous nuclear reactions, may represent up to 40% of the total non-em energy, with large event-to-event fluctuations. These fluctuations, which have no equivalent in em showers, determine the ultimate limit on the precision with which the energy of showering hadrons can be measured. In practice, fluctuations in the energy sharing between the two mentioned shower components also play an important role, especially in non-compensating calorimeters (see Section 3).

Another aspect of the nuclear reactions through which much of the non-em shower energy is deposited in the absorber

structure with consequences for calorimetry is the production of very densely ionizing particles. These may either be measured with very low efficiency, or lead to anomalously large signals in some calorimeters (Section 2.4).

2.2. Hadronic shower profiles

The appropriate length scale of hadronic showers is the nuclear interaction length (λ_{int}), which is typically much larger than the radiation length (X_0) [7]. Many experiments make use of this fact to distinguish between electrons and hadrons on the basis of the energy deposit profile and signal shape in their calorimeter system. This is illustrated in Fig. 1. Since the ratio λ_{int}/X_0 is proportional to Z , particle identification on this basis works best for high- Z absorber materials. Lead and depleted uranium, for which this ratio reaches values of 30, are therefore popular choices for the absorber material in preshower detectors and the em section of a longitudinally segmented calorimeter.

Just as for the detection of em showers, high-resolution hadron calorimetry requires an average longitudinal containment better than 99%. In iron and materials with similar Z , which are most frequently used for hadron calorimeters, 99% longitudinal containment requires a thickness ranging from $3.5\lambda_{\text{int}}$ at 10 GeV to $7\lambda_{\text{int}}$ at 100 GeV. Fig. 2a shows how these numbers change when the containment requirement is relaxed to 95%.¹ Fig. 2b shows that 95% lateral containment requires a radius of $1.5\text{--}2\lambda_{\text{int}}$. Interestingly, the average lateral shower leakage fraction from a given calorimeter decreases at increasing energy. This is the result of increased π^0 production. The large event-to-event fluctuations in π^0 production are also responsible for the fact that the hadronic energy resolution is more sensitive to the effects of side leakage than the em energy resolution. Hadronic energy resolutions of 1% require not only longitudinal shower containment at the 99% level, but also lateral containment of 98% or better.

2.3. Characteristics of the em shower component

Energetic π^0 s and other mesons that decay into photons may be produced throughout the absorber volume, and not exclusively

¹ Fig. 2a is based on data from the CDHS experiment [10]. More recent data [12] suggest that iron-based calorimeters have to be significantly deeper to contain 99% of the shower energy. However, the (ATLAS) detector used for the latter studies had a much coarser longitudinal sampling ($1.5\lambda_{\text{int}}$ vs $0.3\text{--}0.7\lambda_{\text{int}}$ for CDHS) and was mainly focused on leakage beyond great depths.

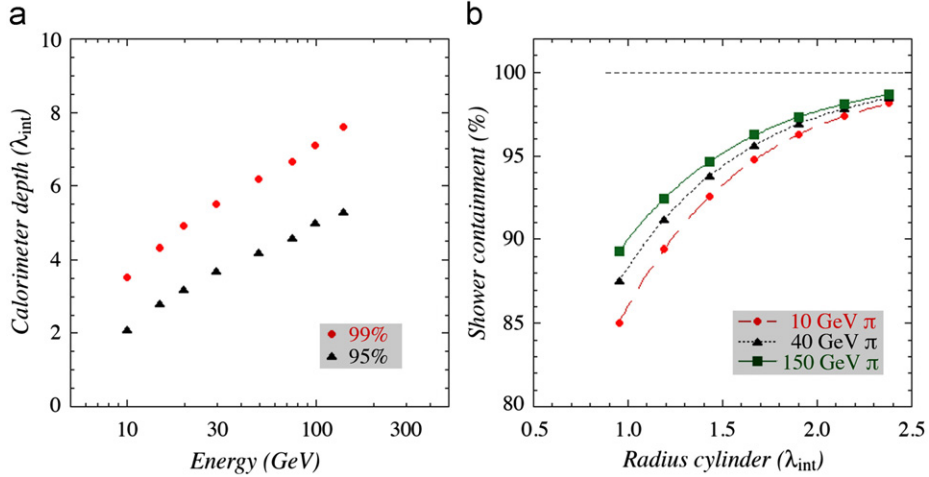


Fig. 2. Size requirements for hadronic shower containment. The depth of an iron-based calorimeter needed to contain pion showers, on average, at the 95% or 99% level, as a function of the pion energy (a) [10]. Average lateral containment of pion-induced showers in a lead-based calorimeter as a function of the radius of an infinitely deep cylinder around the shower axis, for three different pion energies (b) [11].

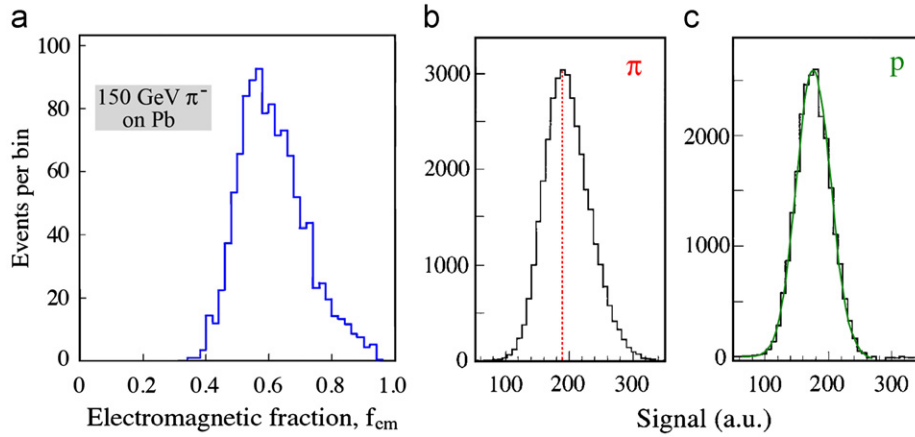


Fig. 3. Event-to-event fluctuations in the em fraction of 150 GeV π^- showers in lead [18] (a). Signal distributions for 300 GeV pion (b) and proton showers (c) in a copper-based calorimeter [21].

in the em calorimeter section. They lead to local regions of highly concentrated energy deposits (see Fig. 22). Therefore, there is no such thing as a “typical hadronic shower profile” [13]. This feature affects not only the shower containment requirements, but also the calibration of longitudinally segmented calorimeters [14,15], and the applicability of particle flow analysis (PFA) techniques [16,17] in which one tries to improve the quality of calorimetric energy measurements of jets with a precision tracker (see Section 7).

The characteristics of the em shower component have also important consequences for the energy resolution, the signal linearity and the response function. These consequences are discussed in Section 3. The average fraction of the total shower energy contained in the em component has been measured to increase with energy following a power law [18,19], confirming an induction argument made to that effect [20]:

$$\langle f_{\text{em}} \rangle = 1 - (E/E_0)^{k-1} \quad (1)$$

where E_0 is a material dependent constant related to the average multiplicity in hadronic interactions (varying from 0.7 GeV to 1.3 GeV for π -induced reactions on Cu and Pb, respectively), and $k \sim 0.82$. For proton-induced reactions, $\langle f_{\text{em}} \rangle$ is typically significantly smaller, as a result of baryon number conservation in the shower development (Section 5.2) [21]. In addition, event-to-

event fluctuations are smaller and more symmetrically distributed around the average value, as illustrated in Fig. 3.

2.4. Effects of nuclear interactions

In commonly used absorbers, such as iron, copper or steel, typically $\sim 80\%$ of the non-em energy is deposited through nuclear reactions. Apart from the nuclear binding energy losses, which constitute the invisible energy discussed above, these reactions produce densely ionizing particles, mainly protons, but also nucleon aggregates such as α particles. In addition, large numbers of evaporation neutrons are released with typical kinetic energies of a few MeV.

Fig. 4 shows an example of such a reaction, made visible in a nuclear emulsion. The reaction is induced by a proton with a kinetic energy of 160 MeV. In total, eight densely ionizing particles are released, as well as an unknown number of neutrons, which of course did not leave tracks. Based on the range of the charged particles, they are most likely protons with kinetic energies of a few MeV. The specific ionization of such protons is three orders of magnitude larger than for minimum ionizing particles.

In calorimeters, such nuclear reactions may have profound effects. In scintillating crystals, an event such as the one shown

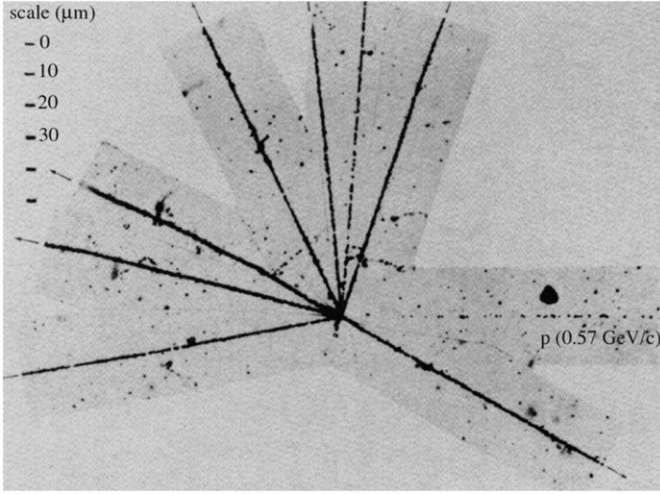


Fig. 4. Nuclear interaction induced in an emulsion by a proton with a kinetic energy of 160 MeV. Photo courtesy CERN.

in Fig. 4 would produce almost no signal, because of the saturation effects for densely ionizing particles (Birks' constant [22]). However, in other types of calorimeters such events may give rise to signals that are interpreted as energy deposits of tens of GeV or more. For example, in sampling calorimeters based on gas as active medium, e.g., in wire chambers, the sampling fraction is typically of the order 10^{-5} . This means that when a 100 GeV hadron is absorbed in this structure, only of the order of 1 MeV of energy is deposited in the form of gas ionization by all the charged shower particles combined. This sets the energy scale of the calorimeter. A particle for which the charged shower components generate a total ionization of 0.5 MeV in this calorimeter will thus be attributed an energy of 50 GeV. If now a MeV-type neutron produced in the shower development underwent elastic scattering off a hydrogen nucleus in the gas (which may contain isobutane or some other hydrocarbon compound) and transferred 0.2 MeV of kinetic energy to that proton, then the ionization of the gas caused by this recoil proton would generate a signal equivalent to that of a 20 GeV showering hadron, assuming that the recoil proton stopped in the gas. This is a reasonable assumption since the range of a 0.2 MeV proton in the gas mixtures used in wire chambers is typically 2.0–2.5 mm, less than the typical gap width of such chambers. Since elastic neutron–proton scattering is a local event, the result would be a large signal in only one calorimeter cell. And since shower neutrons usually undergo many elastic scattering processes before being captured, the scattering process taking place in the gas may occur anywhere in the calorimeter. In other words, lead to hot spots anywhere in the detector. This phenomenon, first observed by L3 [23], was known as the “Texas Tower effect”, and it greatly complicated the experiments in which it played an important role, e.g., CDF [24,25].

Densely ionizing particles such as those shown in Fig. 4 may also produce signals that are five orders of magnitude larger than those from scintillation photons in photosensors such as avalanche photodiodes. The resulting signal from the nuclear fragments could then be interpreted as an energy deposit of the order of 100 GeV.² Whereas events such as those shown in Fig. 4 are typically associated with hadronic shower development in or near

the detector cell (e.g., crystal) where the hot spot occurs, elastic neutron scattering in close proximity of an APD may cause anomalously large signals that are not at all associated with hadronic shower development in the crystal where it is observed. Such signals may even be caused by neutrons produced in events that occurred in previous bunch crossings in collider experiments, since it may take hundreds of nanoseconds before a neutron has lost enough energy in a series of elastic collisions to be harmless.

3. Effects of non-compensation

Let us define the calorimeter *response* as the average conversion efficiency from deposited energy to generated signal, and normalize it to electrons. The responses of a given calorimeter to the em and non-em hadronic shower components, e and h , are usually not the same, as a result of invisible energy loss and a variety of other effects. Such calorimeters are called *non-compensating*, i.e. their e/h ratio, a constant characteristic for the calorimeter in question, differs from unity. Since their response to pions, $\langle f_{em} \rangle + (1 - \langle f_{em} \rangle)h/e$, is energy dependent (Eq. (1)), they are intrinsically non-linear.

Event-to-event fluctuations in f_{em} are large and non-Poissonian. If $e/h \neq 1$, these fluctuations tend to dominate the hadronic energy resolution as reflected in the signal distributions (Figs. 3 and 23a). It is often assumed that the effect of non-compensation on the energy resolution is energy independent (“constant term”). This is incorrect. The effects of fluctuations in f_{em} on the energy resolution (Fig. 5a) can be described by a term that is very similar to the one used for the energy dependence of its average value (Eq. (1)). This term should be added in quadrature to the $E^{-1/2}$ scaling term which accounts for all Poissonian fluctuations:

$$\frac{\sigma}{E} = \frac{a_1}{\sqrt{E}} \oplus a_2 \left[\left(\frac{E}{E_0} \right)^{l-1} \right] \quad (2)$$

where the parameter $a_2 = |1 - h/e|$ is determined by the degree of non-compensation [26]. Eq. (2) is represented by the solid curve in Fig. 5b, for parameter values that are typical for many calorimeters. In the energy range covered by the current generation of test beams, i.e. up to 400 GeV, it runs almost parallel to the dotted line, which represents a single stochastic term with a somewhat larger coefficient ($a_1 = 0.55$ instead of 0.50). This solves an old mystery, since it means that experimental data might also be described by an expression of the type:

$$\frac{\sigma}{E} = \frac{a_1}{\sqrt{E}} + a_2 \quad (3)$$

i.e. a linear sum of a stochastic term and a constant term. Many sets of experimental hadronic energy resolution data exhibit exactly this characteristic.

4. Calibration of calorimetry systems

The energy resolution of calorimeters is usually determined from the width of the signal distribution for monoenergetic beam particles. However, this is only correct if the mean value of that distribution reproduces the beam energy for all energies. Meeting this requirement, which is the purpose of the calibration procedure, is highly non-trivial. As we enter the TeV domain and expect resolutions at the level of a few percent, meeting this requirement is correspondingly harder. Calibration problems are often grossly underestimated [15]. In this review, we only highlight some aspects using examples taken from practice. The problems become rapidly worse as the calorimeter is subdivided into more

² The scintillation light produced by em showers developing in PbWO_4 crystals read out by APDs generates typically a few thousand photoelectrons per GeV deposited energy.

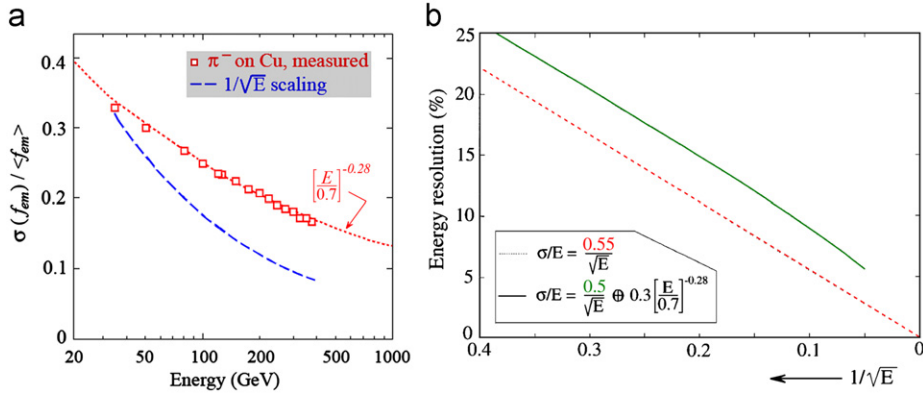


Fig. 5. Energy dependence of the fractional width of the f_{em} distribution. Shown are the results of measurements [19] and the expected dependence for fluctuations governed by Poisson statistics (a). The hadronic energy resolution calculated for a typical non-compensating calorimeter in the energy regime up to 400 GeV (the solid line), and calculated with only a sole stochastic term, with a slightly larger scaling constant (b) [2].

and more longitudinal segments. However, unsegmented calorimeters are not without calibration problems either.

4.1. Unsegmented calorimeters

One of the advantages of such a calorimeter system is that there is only one section to calibrate. The energy scale is set with electrons. Measurements with pions of different, known energies, covering preferably as large an energy range as possible, make it possible to determine e/h and $\langle f_{em} \rangle$. With this information, the signal from an arbitrary pion (E_{em}) can be converted into its, on average correct, energy (E_{π}):

$$E_{\pi} = E_{em}[h/e + \langle f_{em} \rangle(1-h/e)]^{-1} \quad (4)$$

in a few iterations in which $\langle f_{em} \rangle$ is adjusted.

A similar procedure can provide the tools for reconstructing jet energies. In the absence of “jet test beams” of known energy, the only way to determine $\langle f_{em} \rangle$ for jets is by means of a suitable fragmentation function (which gives the fraction of the jet energy carried by photons and other fragments developing em showers) and the energy dependence of $\langle f_{em} \rangle$ for the individual charged jet fragments.

A fundamental problem arises from the fact that not all hadrons have the same $\langle f_{em} \rangle$ values. For example, in highly non-compensating calorimeters, differences in excess of 10% have been measured between the $\langle f_{em} \rangle$ values for 0.3 TeV proton and pion-induced showers. Unless one has another way to establish the particle type, this phenomenon will inevitably lead to systematic energy mismeasurements. Fortunately, the importance of such effects rapidly decreases as the e/h value gets less extreme, or the number of particles in a jet increases.

4.2. Segmented calorimeters

Most calorimeters consist of separate em and hadronic sections. Previous studies have indicated the importance of calibrating both sections in the same way [14,15]. However, even in that case, problems arise when the two sections have different e/h values. This became very clear in studies of the hadronic performance of the CMS barrel calorimeter, which consists of an em section made of $PbWO_4$ crystals ($e/h \approx 2.5$), and a brass/plastic-scintillator hadronic section ($e/h \approx 1.4$). Also the em and hadronic sections of ATLAS have different e/h values, but the differences are much smaller in that case.

The hadronic performance of the CMS calorimeter system was systematically studied (see Section 5.2) where both sections were calibrated with 50 GeV electrons [27]. Fig. 6 shows that the

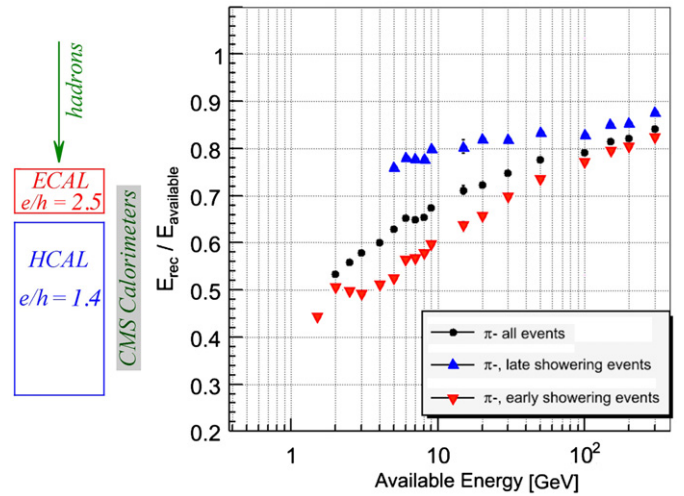


Fig. 6. The response to pions as a function of energy, for the CMS barrel calorimeter. The events are subdivided into two samples according to the starting point of the shower, and the response is also shown separately for these two samples [27]. The normalization is based on the response to electrons (see Section 5.2).

response to pions, represented by the black dots, is non-linear. This non-linearity is especially evident below 10 GeV, which is important since pions in this energy range carry a large fraction of the energy of jets at the LHC. More troublesome is the fact that the response depends on the starting point of the showers. The figure shows results for two event samples, selected on that basis: showers starting in the em section (red) or in the hadronic section (blue). At low energies, the response is more than 50% larger for the latter (penetrating) events. In practice, in an experiment, it is often hard/impossible to determine where the shower starts, especially if these pions are traveling in close proximity to other jet fragments (e.g., photons from π^0 decay) which develop showers in the em section.

4.3. Calibration and hadronic signal linearity

Hadronic signal non-linearities and starting point dependence of the response are a general characteristic of non-compensating calorimeter systems, although the effects are usually not as large as shown in Fig. 6. Many calibration schemes used in practice set the energy scale of the em calorimeter section with electrons, while the hadronic section is calibrated with pions that penetrate

the em section without a nuclear interaction and deposit their (almost) entire energy in the hadronic section. Other schemes choose the calibration constants for the hadronic section on the basis of a minimization of the width of the total signal distribution. It has been demonstrated experimentally that one of the consequences of these schemes is an increase in the hadronic signal non-linearity, over and above the non-linearity that would result from a correct calibration scheme [14,28] and such calibration procedures need to be critically evaluated in each case.

Hadronic signal non-linearity is bad, especially when it comes to jet detection. It is bad because it makes the reconstructed energy dependent on the jet topology: A jet with a leading particle that carries a large fraction of the energy of the fragmenting object will be reconstructed with a different energy than a jet whose energy is more evenly divided among the different constituent particles. This phenomenon will, for example, lead to different calorimeter responses to gluon and quark jets of the same energy, because of the different composition of such jets. Calibration schemes that increase such differences should be avoided, but in practice this is not the case since one is usually focused on the energy resolution. However, it should be realized that the width of a signal distribution is only an indication of the resolution (*i.e.* the precision with which the energy of an event can be determined) if the central value of the distribution has the correct energy. The effects of signal non-linearity invalidate this presumption.

4.4. Electromagnetic showers in segmented calorimeters

Response non-uniformity is not only a problem for hadron showers, it also affects electrons and photons that develop showers in a longitudinally segmented em (sampling) calorimeter. The basic reason is that the response of a given calorimeter structure depends on the stage of the developing showers. For example, in calorimeters consisting of high-Z absorber material (*e.g.*, lead) and low-Z active material (plastic, liquid argon), the response may vary by as much as 25–30% over the volume in which the absorption takes place. In the early stage of its development, the shower still resembles a collection of mips, but especially beyond the shower maximum, the energy is predominantly deposited by soft (< 1 MeV) γ s. The latter are much less efficiently sampled than mips in this type of structure, where dominant processes such as photo-electric effect and Compton scattering strongly favor the high-Z absorber material [2].

The fact that the em shower sampling fraction decreases as the shower develops may have very important practical consequences. These include:

- Systematic mismeasurement of energy [29];
- Electromagnetic signal non-linearity [30], and
- Differences in response to showers induced by electrons, photons and π^0 s [31].

These issues are especially relevant in longitudinally segmented calorimeters, where one has to decide which calibration constants to assign to the different segments.

A recent example of an experiment that has to deal with this intercalibration issue is ATLAS, whose Pb/LAr ECAL consists of three longitudinal segments. Fig. 7 shows how the sampling fraction evolves as a function of depth, in an energy dependent way. Elaborate Monte Carlo simulations played a crucial role in ATLAS' solution of the intercalibration problems, for which they developed a very sophisticated procedure, based on a variety of energy-dependent parameters. This procedure was tested in detail with Monte Carlo events and yielded both excellent signal linearity and good energy resolution [32]. Typically, in more empirical approaches to this problem, only one of these

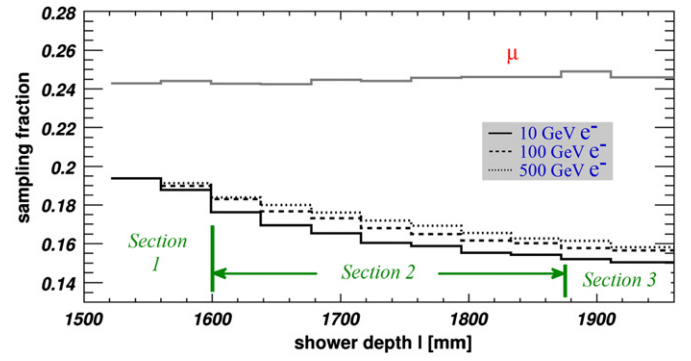


Fig. 7. Evolution of the sampling fraction for electron showers of different energies in the three longitudinal segments of the ATLAS em calorimeter [32].

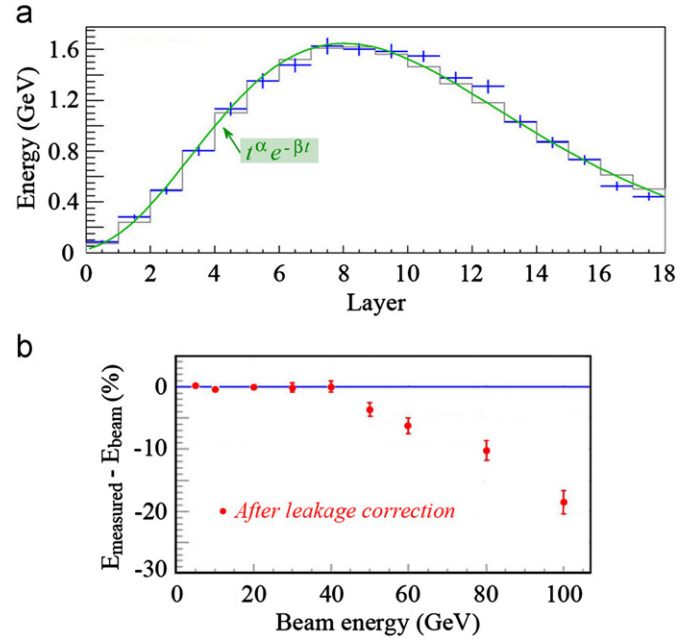


Fig. 8. Average signals for 100 GeV electrons in the 18 longitudinal sections of the AMS lead/scintillating fiber calorimeter (a). Average difference between the measured energy and the beam energy, after leakage corrections based on extrapolation of the fitted shower profile (b). Data from Ref. [29].

performance characteristics is pursued in isolation, and the results are far from optimal [2,15].

The (inter) calibration problems get rapidly more complicated as the number of longitudinal calorimeter segments increases. Fig. 8 shows data from the AMS em calorimeter, which consists of 18 Pb layers (each $\sim 1X_0$ thick), interleaved with plastic scintillating fibers. All 18 longitudinal segments of this detector are thus identical in structure. They are also calibrated in exactly the same way, with minimum-ionizing particles (mips), which deposit on average 11.7 MeV in each layer. Fig. 8a shows the average signals from 100 GeV electron showers developing in this calorimeter. These signals were translated into energy deposits based on the mip calibration. The measured data were fitted to a Γ -function and at high energies, where the showers were not fully contained, the average leakage was estimated by extrapolating this fit to infinity. As shown in Fig. 8b, this procedure systematically underestimated the leakage fraction, more so as the energy (and thus the leakage) increased. The reason for this is clear. Since the sampling fraction decreases as the shower develops, a procedure in which the relationship between measured signals and the

corresponding deposited energy is the same for each segment will cause the energy leakage to be systematically underestimated, more so if that leakage increases. What is not so clear is how to solve this complicated problem.

5. Calorimeters at the LHC

The ATLAS and CMS calorimeters started to take useful data for physics analyses as the LHC began stable operations at a center of mass energy of 7 TeV in 2010. These calorimeters are quite different in technical aspects, but the performance requirements deriving from the physics that is pursued are very similar. We concentrate on these two, especially on the performance characteristics of the combined em and hadronic calorimeters.

5.1. ATLAS

The hadronic section of the ATLAS calorimeter (TileCal) is a sampling iron/plastic-scintillator detector, located in the region $|\eta| < 1.7$. This hadronic calorimeter extends from an inner radius of 2.28 m to an outer radius of 4.25 m. Each section is segmented into 64 azimuthal sections, referred to as modules, subtending $\Delta\phi = 2\pi/64 \approx 0.1$. The scintillator plates are oriented perpendicularly to the colliding beam axis, and are radially staggered in depth as schematically shown in Fig. 9. By the grouping of WLS fibers to specific PMTs, modules are segmented in η and in radial depth. In the direction perpendicular to the beam axis, the three radial segments span 1.5, 4.1 and 1.8 λ_{int} in the barrel and 1.5, 2.6, 3.3 λ_{int} in the extended barrels. The resulting typical cell dimensions are $\Delta\eta \times \Delta\phi = 0.1 \times 0.1$ (0.1×0.2 in the last segment). This segmentation defines a quasi-projective tower structure, where the deviations from perfect projectivity are small compared to the typical angular extent of hadronic jets. Altogether, TileCal

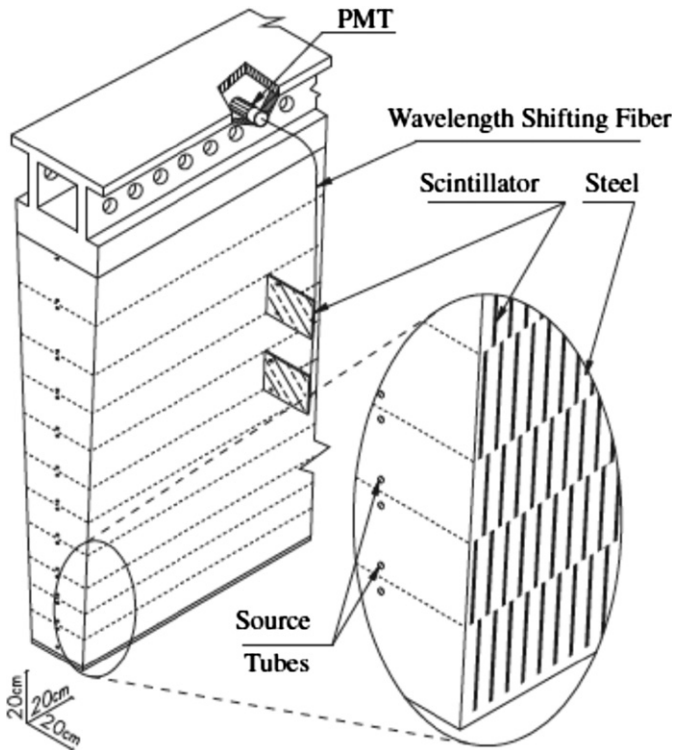


Fig. 9. The mechanical structure of the ATLAS TileCal module. The plastic scintillator tiles are read out from both sides with wavelength shifting fibers into separate PMTs. The staggered absorber/scintillator and the radioactive source tubes are shown on the right.

comprises 4672 readout cells, each equipped with two PMTs that receive light from opposite sides of every tile (see Refs. [33,11] for detailed description). The end-cap and forward hadronic calorimeters ($1.5 \leq \eta \leq 4.9$) are based on LAr technology.

Motivated by the fact that a large fraction of the jet energy is carried by particles of a few GeV, the ATLAS collaboration tested their electromagnetic (Pb/LAr) and hadronic calorimeter systems with low momentum (3–9 GeV/c) particle beams [34] and in a separate series of measurements with particles of higher momenta (20–350 GeV/c) [35]. Both sections were calibrated using electrons to set a common energy scale and the shower energy in the calorimeter was determined as the sum of raw signals from these two sections, $E_{\text{raw}} = E_{\text{raw}}(\text{em}) + E_{\text{raw}}(\text{had})$. The $E_{\text{raw}}(\text{em})$ term comprised the sum of the energy deposited in the front, middle, and back samples of the em section, and the $E_{\text{raw}}(\text{had})$ represented the sum of signals from the first and second samples of the hadronic section for low energies. In reconstructing the energy of the event, several conditions were applied: no pre-sampler contribution was added to the em signal, and only calorimeter cells with energy depositions larger than twice the standard deviation of the electronic noise were included in the sum. No corrections due to shower containment, non-compensation, or dead material were applied. The signal distributions for low energies are shown in Fig. 10, and Fig. 11 shows the response to hadrons as a function of energy. Both figures also contain the results of GEANT MC simulations. Fig. 11 reveals a strong signal non-linearity. The relative response difference between the measured and simulated data depends on the beam energy and the impact point on the calorimeter (η_{beam}). The simulation overestimates the signal by 5–10% at low momenta (3–9 GeV/c), while the energy resolution is underestimated by 15% at 3 GeV and 5% at 9 GeV. In general, the agreement is somewhat better at higher energies but degrades at higher η_{beam} .

Beam tests with TileCal alone provided some interesting results [11]. In Fig. 12a, the responses are plotted without leakage corrections, and in Fig. 12b with longitudinal and transverse leakage corrections. The response of the TileCal to pions was parametrized as $E(\pi)/E_{\text{beam}} = (1-f_h) + (h/e)f_h$ and fitted to experimental data. When Figs. 11 and 12 are compared, it becomes clear that most of the signal non-linearity is induced by the Pb/LAr ECAL calorimeter: in the 20–350 GeV range, $\sim 10\%$ non-linearity of TileCal alone increases to $\sim 20\%$ in the combined system. At low energies, the non-linearity is even more dominated by the ECAL.

When the TileCal hadronic energy resolution is parametrized in the customary fashion $\sigma/E = a/\sqrt{E} \oplus b$, the stochastic term $a = (52.9 \pm 0.9)\% \text{ GeV}^{-1/2}$ and the constant term $b = 5.7 \pm 0.2\%$. The noise level is small at all energies and is not considered in the parametrization. There is a good agreement at higher energies between the GEANT4 simulation and measurements.

Another interesting result that emerged from the TileCal beam tests is the response difference between pions and protons. As the particle energy increases, the response ratio decreases in the tested energy range (Fig. 13a); however, the energy resolution for protons is 15–20% better (Fig. 13b). This is a result of the fact that π^0 production fluctuates less from event to event as a consequence of baryon number conservation. This effect was first observed in a quartz fiber calorimeter prototype for the CMS forward calorimeter [21] and was also measured for the CMS calorimeter systems [36].

5.2. CMS

The CMS barrel calorimeter system consists of a fully active em section, made of PbWO_4 crystals, while the hadronic section is a sampling structure consisting of alternating brass and scintillator

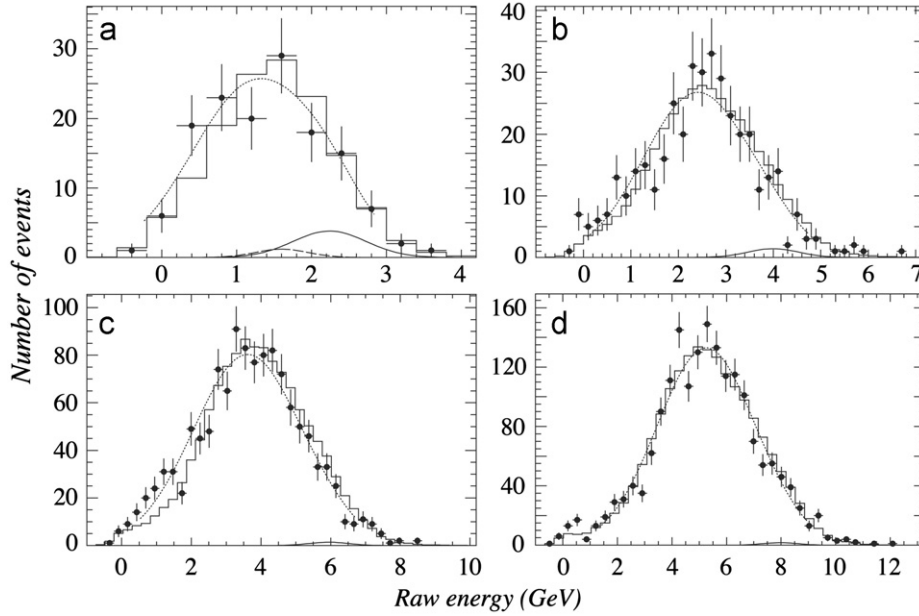


Fig. 10. Distribution of the reconstructed energy (E_{raw}) for the combined ATLAS em+had system for (a) 3 GeV, (b) 5 GeV, (c) 7 GeV and (d) 9 GeV pions at $\eta_{\text{beam}} = 0.35$ [34]. The full points represent the measured data. The dashed curves correspond to a fit to the data in a region $\pm 2\sigma$ around the mean value where the electron and muon contaminations in the beam are taken into account. The solid curve represents the expected contribution of the electron contamination in the beam. At 3 GeV, the long-dashed curve shows the expected contribution from the decay muons. The histograms correspond to the prediction of the GEANT4 v9.1 simulation with the QGSP_BERT physics list.

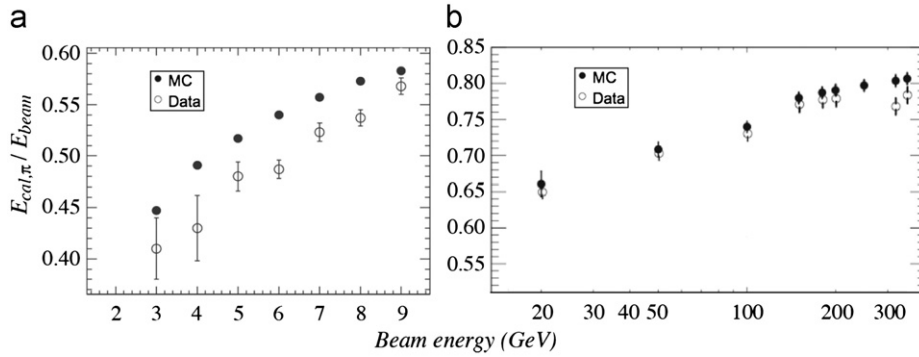


Fig. 11. The measured E_{π}/E_{beam} ratio (for $\eta_{\text{beam}} = 0.35$) for the combined ATLAS system at low (a) [34] and high energies (b) [35]. The error bars include statistical as well as systematic errors added in quadrature. The GEANT4 prediction is represented by the black circles.

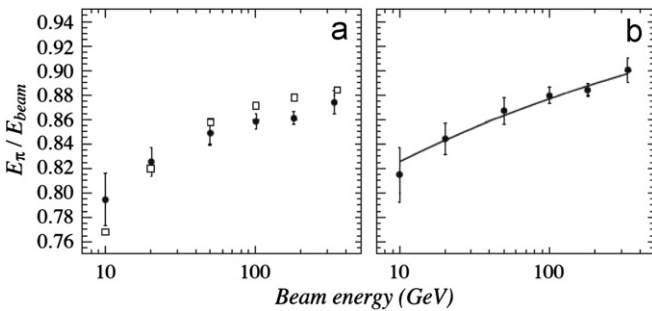


Fig. 12. The response of TileCal (at $\eta_{\text{beam}} = 0.35$) to pions as a function of pion energy before (a) and after (b) corrections for the effect of shower leakage. The squares represent GEANT4 predictions. The curve shows the result of a fit to Eqs. (1) and (4) with $e/h = 1.33$, $E_0 = 1$ GeV and $k=0.85$ [11].

plates. These sections have e/h ratios of 2.5 and 1.4, respectively. Because of this large difference between the e/h values of the em and hadronic sections, the combined CMS calorimeter system poses interesting challenges [36]. The CMS HCAL covers the pseudorapidity range $-1.3 < \eta < 1.3$ and consists of 36 identical

azimuthal brass wedges ($\Delta\phi = 20^\circ$), which form two half-barrels. Each wedge is further segmented into four azimuthal ($\Delta\phi = 5^\circ$) sectors. The plates are bolted together in a staggered geometry resulting in a configuration that contains no projective passive material for the full radial extent of a wedge. The interleaved scintillator plates are divided into 16 η sectors, resulting in a segmentation of $(\Delta\eta, \Delta\phi) = (0.087, 0.087)$. The total absorber thickness at 90° is $5.82 \lambda_{\text{int}}$. The effective thickness increases with the polar angle to $10.6 \lambda_{\text{int}}$ at $|\eta| = 1.3$. The PbWO_4 ECAL in front adds $\sim 1.1 \lambda_{\text{int}}$ independent of η . Technical details of the CMS HCAL can be found in Refs. [37,38].

The signal distributions for 5 and 100 GeV/c π^- beam particles are displayed in Fig. 14. A sizable fraction of pions interact in the em section. This can be concluded from the signal distributions in Fig. 14a and d which exhibit a clear mip-peak caused by particles that penetrate the ECAL without starting a shower, as well as a broad distribution of larger signals caused by pions that did start a shower. The signals in the HCAL show complementary distributions, i.e. small signals for the early showering particles and larger signals for the ones that penetrated the ECAL.

CMS has performed a detailed study of the response of their calorimeter system to particles in the energy range below 10 GeV.

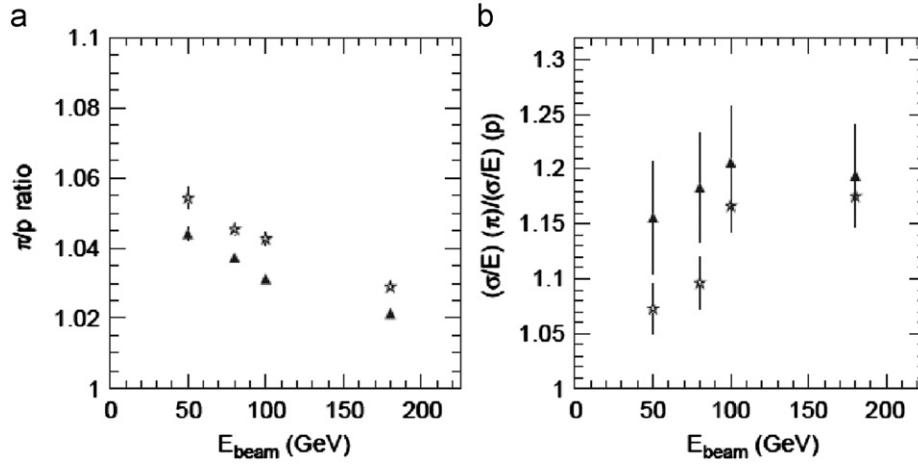


Fig. 13. The energy dependence of the π/p ratio (a) and ratio of the energy resolutions for pions/protons (b). Experimental data are shown with full triangles. The simulation results *GEANT4* (version 5.2, with the QGSP model but without the Bertini intranuclear cascade model) are represented by stars [11].

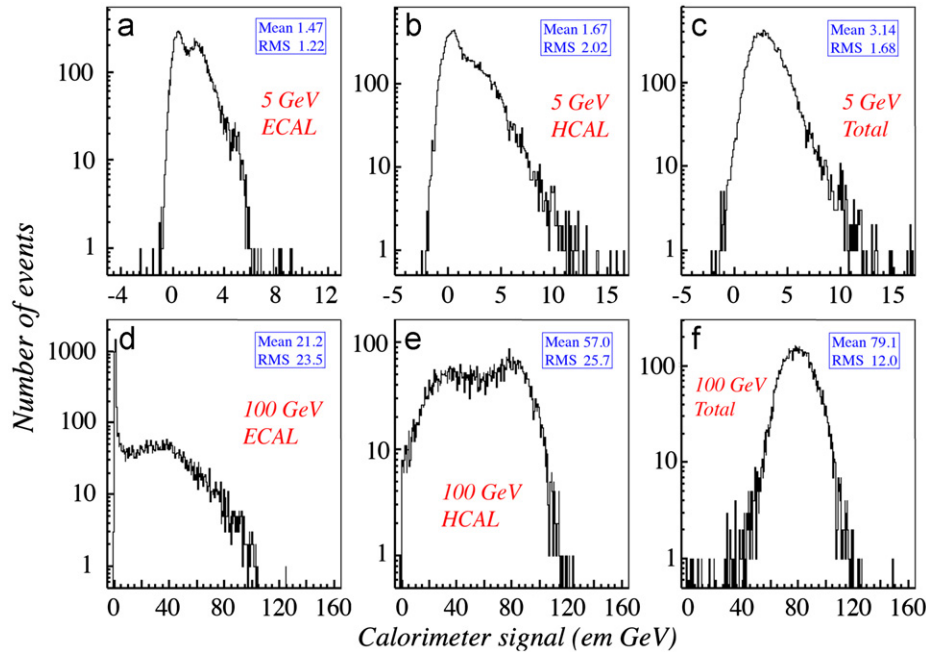


Fig. 14. The signal distributions for 5 and 100 GeV/c negative pions are shown for the CMS em calorimeter section (a and d), the hadronic calorimeter section (b and e), and the combined system (c and f), which also includes longitudinal energy leakage [27].

Because of the importance of these particles for jet response, we elaborate in the following the results of these studies. Fig. 15 shows the response of the CMS calorimeters to a variety of particles. The data are normalized to the electron response, for both sections of the calorimeter. In Fig. 15a where the calorimeter response is plotted as a function of beam momentum, large differences between the different particles are apparent, especially at low momenta. For example, at 5 GeV/c, the antiproton response is $\sim 70\%$ of the electron response while the responses to charged pions and protons are 62% and 47% of the electron response, respectively. However, we want to emphasize that a calorimeter responds to available energy, which is different for different particles carrying the same momentum. For pions and kaons, the available energy is their kinetic energy plus their mass. For protons, it is the kinetic energy, and for antiprotons, the available energy for a calorimetric signal equals the kinetic energy plus twice the proton rest mass. In Fig. 15b, the same data are plotted as a function of available energy. In first approximation, one would expect the response to be independent of the hadron

type when the data are represented this way. However, this is not the case.

For example, the response to π^+ is systematically larger than the π^- response, more so as the energy decreases. This can be understood from the characteristics of the charge exchange reactions, $\pi^+ + n \rightarrow \pi^0 + p$ (I) and $\pi^- + p \rightarrow \pi^0 + n$ (II). In these reactions, a large fraction of the pion energy is carried by the final-state π^0 , which develops electromagnetic showers. Therefore, the calorimeter response to pions interacting this way is close to 1. Since the target material (PbWO_4) contains about 50% more neutrons than protons, the relative effect of reaction (I) will be larger than that of reaction (II), and therefore, the calorimeter response to π^+ should be expected to be larger than the π^- response.

The response to protons is systematically smaller than the pion response. We already discussed this effect in the context of the ATLAS measurement (Fig. 13). In the CMS quartz fiber calorimeter this effect caused a response difference in excess of 10% [21]. Since the e/h values of ECAL+HCAL are smaller than for

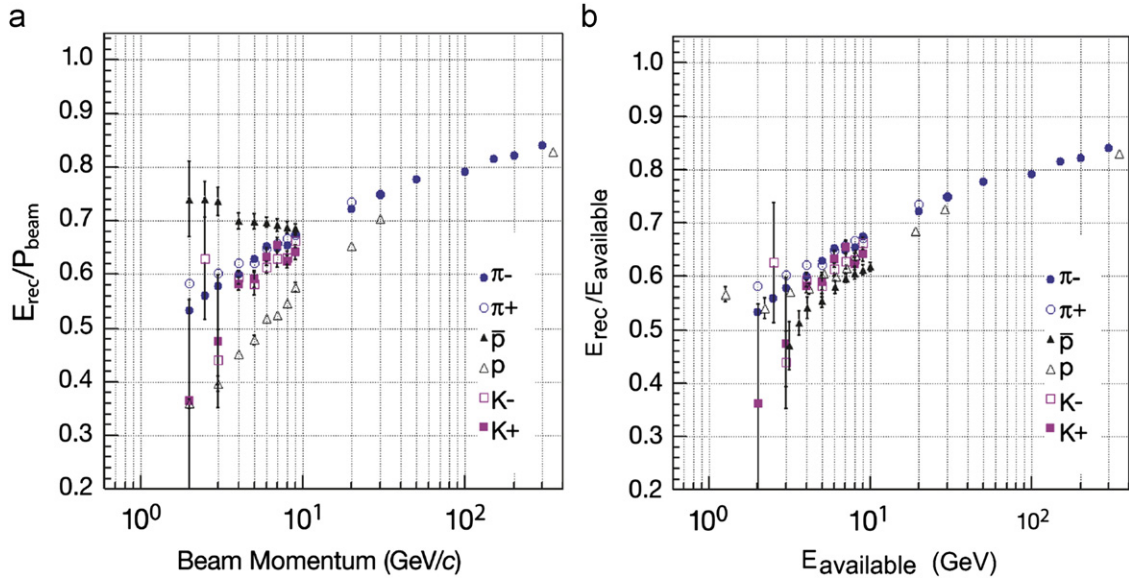


Fig. 15. The response of the combined calorimeter systems to different particles is shown as a function of beam momentum (a) or as a function of available energy (b) [36]. The response of both ECAL and HCAL is normalized to that for electrons.

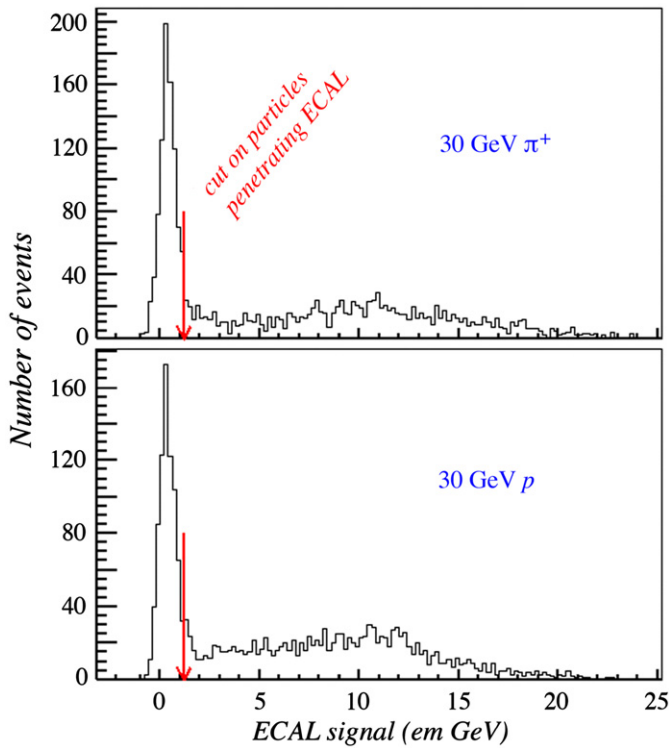


Fig. 16. The signal distributions from the CMS ECAL for 30 GeV/c pions (top) and protons (bottom). The arrow indicates where the cut is applied (1.2 GeV) to separate the penetrating pions and protons from the interacting ones [36].

the quartz fiber calorimeter, the effects are correspondingly smaller, but nevertheless significant.

Since the total cross-section for baryon induced interactions is larger than for pions, a larger fraction of the baryons start showering in the ECAL. This is illustrated in Fig. 16, which shows that 41% of the pions penetrate the ECAL without starting a shower, versus only 35% for protons. The effective thickness of the ECAL is thus $1.05\lambda_{\text{int}}$ for protons and $0.89\lambda_{\text{int}}$ for pions. Since the total cross-sections for protons and antiprotons are about the same, the same holds for the effective ECAL thickness.

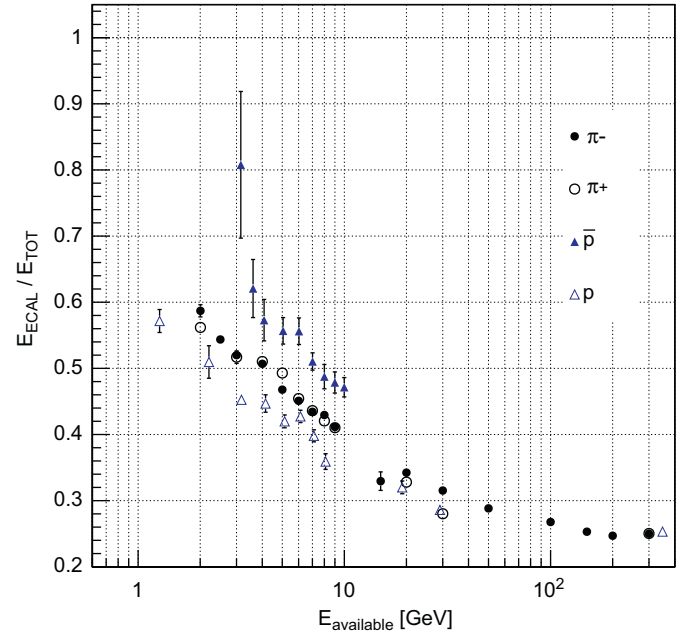


Fig. 17. The fraction of energy deposited in the CMS ECAL as a function of the available energy for charged pions and (anti)protons [27].

The previous two points make it possible to understand Fig. 17, which shows the average energy sharing between the ECAL and HCAL for hadronic showers. The fraction of the energy recorded by the ECAL increases from $\sim 25\%$ at the highest energies to $\sim 60\%$ at 2 GeV. Remarkably, at the same energies, protons deposit on average less than pions in the ECAL, while antiprotons deposit more than pions. Antiprotons start their showers, on average, earlier than pions and therefore a larger fraction of the energy ends up in the ECAL. At first sight, one would expect the same for proton induced showers. However, when a proton interacts in the ECAL, the final state should contain two baryons, which limits the energy available for π^0 s. And since the ECAL, for all practical purposes, only sees the π^0 component of the showers, this effect suppresses the proton signal in the ECAL, despite the fact that

protons are more likely to start their showers in the ECAL compared to pions. The requirements of baryon number conservation do not limit π^0 production for antiproton induced showers. In first approximation, there is in this respect no difference with pion induced showers. Therefore, the ECAL/HCAL energy sharing properly reflects the difference in interaction length in this case.

The effects described above also explain why the antiproton response is systematically smaller than the pion response (Fig. 15b). Antiprotons are more likely to start showering in the ECAL compared to the pions. Pions deposit, on average a larger fraction of their energy in the ECAL. And since the e/h value of the HCAL is smaller than for the ECAL, the pions benefit more from the increased response to the non-em shower components.

In order to study the effects of the very different e/h values of the ECAL and HCAL, the pion event samples were grouped into “early” and “late” starting showers. The distinction was made on the basis of the energy fraction observed in the ECAL. For late starting showers, this energy fraction was chosen such that events in the *mip* peak in the ECAL were selected. These pions thus only lost some energy by ionization in the ECAL and underwent the first nuclear interaction in the HCAL. In early starting events, the pions deposited a larger fraction of their energy in the ECAL. The pion response for these two classes of events is shown as a function of available energy in Fig. 6, together with the overall pion response. For the lowest energies it was not possible to select a clean sample of “late” events, since the *mip* peak was not clearly resolved in the ECAL distribution (see Fig. 14a). Fig. 6 shows an increasing discrepancy between the calorimeter responses to early and late showers as the particle energy decreases. The discrepancy itself reflects the different e/h values. Late showers deposit almost no energy in the ECAL, and therefore their response is determined by the (more compensating) HCAL. Early showers experience the strong (by a factor 2.5) reduction in the response to the non-em shower component deposited in the ECAL. The fact that the discrepancy increases at lower energy reflects the changes in the longitudinal shower profile also observed in the energy sharing plot (Fig. 17). The larger the average fraction of the shower energy deposited in the ECAL, the larger the response discrepancy between showers that start in the ECAL and those that do not.

CMS applies corrections to the signals from the considerably different ECAL and HCAL in reconstructing the energies of hadrons as described in detail in Ref. [36]. Above 5 GeV/c, these corrections lead to an energy resolution of the combined system where the stochastic term equals $84.7 \pm 1.6\%$ GeV^{-1/2} and the constant term is $7.4 \pm 0.8\%$. The corrected mean response remains constant within 1.3% rms.

At the lowest particle energies, the downward trend in the pion response is observed to reverse for early developing showers (see Fig. 6). The minimum response is observed at 4 GeV. A similar effect was observed by the ZEUS Collaboration [39], who also saw the response of their uranium/scintillator calorimeter increase for energies below 5 GeV. The explanation for this phenomenon is the fact that at lower energies, a gradually increasing fraction of the particles range out without inducing any nuclear reaction. Nuclear reactions are responsible for the invisible energy losses that increase e/h and thus reduce the hadronic response. The calorimeter responds to such non-interacting particles in the same way as it responds to muons. Below 2 GeV, where almost all particles are completely stopped in the calorimeter, the response is equal to that of electrons in the ECAL and even larger than that (by a factor *mip/e*) in the HCAL.

6. Simulations

Hadronic shower simulations have been gradually improving as a result of a better understanding of the underlying physics

processes and the availability of more powerful computing resources. One of the most common tools in this regard is GEANT4 [40]. Several different physics lists³ that describe the various physics processes in shower development are now available for GEANT4 V9.2 (currently used in ATLAS and CMS) and V9.3. In the last decade, an extensive validation program has been carried out for the simulation of the LHC detectors [41]. We want to make some general observations for GEANT4 V9.2 with the QGSP_BERT physics list.

1. The calorimeter response is a few percent larger than for experimental data with an unphysical discontinuity between 9.5 and 9.9 GeV due to a transition between two models for charged pions (LEP and BERT models).
2. The simulated energy resolution is slightly ($\sim 10\%$) better than in reality.
3. The longitudinal shower profile is also more compact ($\sim 10\%$) compared to experimental data.
4. Laterally, the simulation results in showers that are $\sim 15\%$ narrower than in reality.
5. For protons, the discrepancy between the simulation and experimental data seems worse than for pions, e.g. the simulation suggests a $\sim 30\%$ shorter shower profile.⁴

Recently, a new physics list called CHIPS (Chiral Invariant Phase Space decay) [42–44] is being recommended by the GEANT4 developers. It gives reasonable shower shapes and a smooth response as a function of particle energy. It may potentially offer the best description of kaon, hyperon and anti-baryon hadronic interactions available in GEANT4. Fig. 18 shows a comparison between the predictions of the energy dependence of a generic Cu/LAr calorimeter's hadronic response. At low energies, the results vary by as much as 50%.

The data from ATLAS and CMS beam tests with the combined em and hadronic calorimeters (thick-target) as well as stand-alone hadronic calorimeters have proven crucial for validation of the recent physics lists. Two different domains (thin- and thick-target) appear critical for further testing of hadronic shower simulations. Measurements of low energy hadronic interactions in tracker detectors (thin-target) may prove useful to further tune the inelastic hadronic cross-sections and final state models. This region is typically the most difficult to simulate correctly. Hopefully, the collision data from the LHC will shed further light and provide useful input for simulations.

Other test material for hadronic shower simulations has been provided by the CALICE collaboration, which has been exploring calorimeters with high granularity, intended for experiments at a future linear collider. It might be possible to study details of the first interaction, correlations between longitudinal and lateral shower shapes and other features of the hadronic showers in these finely segmented systems. In Fig. 19, experimental longitudinal shower profile data are compared with the predictions of various physics lists for 10 GeV π^- s. The hadronic calorimeter in this case consists of 3 cm thick steel plates interleaved by small scintillator tiles of different sizes [45]. The QGSP_BERT list seems to do the best job in describing these experimental data. The other lists either overestimate the energy density at the shower maximum or underestimate the extend of the shower.

³ http://geant4.cern.ch/support/proc_mod_catalog/physics_lists/physicsLists.shtml

⁴ This disagreement seems to be alleviated in V9.3 with physics list FTFP_BERT.

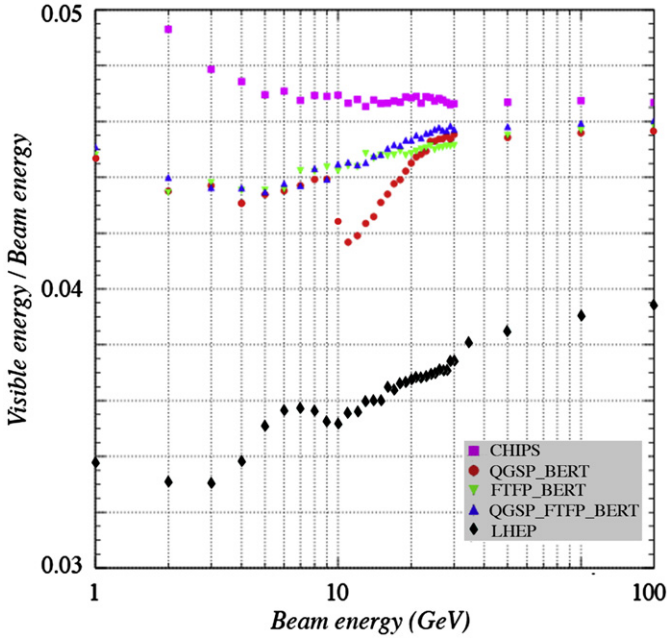


Fig. 18. The ratio of visible to beam energy as a function of the beam energy for π^- s showering in a simplified Cu/LAr calorimeter, as simulated in GEANT4 V9.3.p01 for different physics lists [41]. QGSP_BERT and LHEP show clear discontinuities near 10 GeV, which seem to be absent in CHIPS.

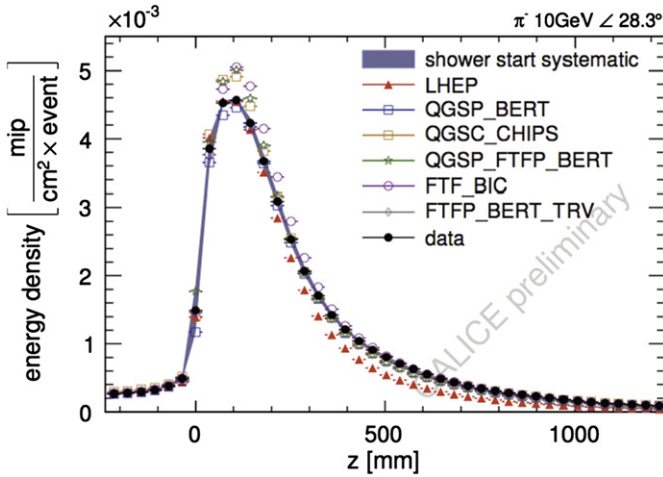


Fig. 19. The longitudinal shower profile measurement with 10 GeV π^- s is contrasted against several physics lists. See Ref. [45] for details.

7. New developments in calorimetry

An often mentioned design criterion for calorimeters at a future high-energy linear e^+e^- collider is the need to distinguish between hadronically decaying W and Z bosons.⁵ The requirement that the di-jet masses of $W \rightarrow q\bar{q}$ and $Z \rightarrow q\bar{q}$ events are separable by at least one Rayleigh criterion implies that one should be able to detect 80–90 GeV jets with a resolution of 3–3.5 GeV. This goal can be, and has been achieved with compensating calorimeters, as illustrated in Fig. 20 [46,47]. However, because of the small sampling fraction required for compensation,

the em energy resolution is somewhat limited in such devices. Also, because of the crucial role of neutrons produced in the shower development, the signals would have to be integrated over relatively large volumes and time intervals to achieve this resolution. This is not always possible in practice. In the following, we discuss some other methods that are currently being pursued to circumvent these limitations.

7.1. Particle flow analysis

One method that has been proposed in this context, the so-called *Particle Flow Analysis* (PFA), is based on the combined use of a precision tracker and a highly granular calorimeter. The idea is that the charged jet particles can be precisely measured with the tracker, while the energy of the neutral particles is measured with the calorimeter. Such methods have indeed successfully been used to improve the mass resolution of hadronically decaying Z^0 s at LEP, to $\sim 7 \text{ GeV}/c^2$ [48]. Several detector concepts studied for the ILC experimental program are based on this method as well [49].

The problem that limits the success of this method is of course that the calorimeter does not know whether the particles it absorbs are electrically charged. Therefore, one will have to correct the calorimeter signals for the contributions of the charged jet particles. Proponents of this method have advocated a fine granularity as the key to the solution of this “double-counting” problem [16].

In order to increase the spatial separation between showers induced by the various jet particles, and thus alleviate the double-counting problem, all concept detectors for the ILC that are based on the PFA principle count on strong solenoidal magnetic fields (4–5 T). Such fields may indeed improve the validity of PFA algorithms, especially at large distances from the vertex, since they open up a collimated beam of particles. After having traveled a typical distance of one meter in a 4 T magnetic field, the trajectory of a 10 GeV pion deviates 6 cm from that of a straight line, i.e. less than one third of a nuclear interaction length in typical calorimeters. The field is also not always beneficial, since it may have the effect of bending some jet particles with a relatively large transverse momentum with respect to jet axis *into* the jet core.

In the absence of reliable Monte Carlo simulations for hadronic shower development [50], the only way to prove or disprove the advocated merits of the proposed PFA methods is by means of dedicated experiments in realistic prototype studies.

The CALICE collaboration has set out to test the viability of these ideas. They have constructed a large calorimeter system, containing about 14,000 readout channels. For the electromagnetic section, silicon pads are used, while the hadronic section is equipped with plastic scintillator tiles or resistive plate chambers. The em section uses tungsten as absorber material, which limits the radial size of em showers. Iron, the absorber material used in the hadronic section, has a Moliere radius that is twice that of tungsten, and a radiation length that is five times larger. This means that the detector volume occupied by an em shower component differs by a factor of 20 in these two sections. This calorimeter has been tested extensively since 2005 in testbeams of electrons, muons and pions.

Technical aspects are elaborated in Refs. [17,51]. A detailed discussion on the performance of the instrument is yet to be published. Fig. 21 shows an event display of a hadronic shower developing in the em/had calorimeter structure. Several single-track elements can be recognized and such track elements were used for the mip calibration of this instrument. The figure also shows the hadronic energy resolution that was achieved on the basis of such a calibration. Around 80 GeV, the energy at which

⁵ An important reaction to be studied is $e^+e^- \rightarrow H^0 Z^0$. By using the hadronic decay modes of the Z^0 (in addition to $\ell^+\ell^-$ decays), an important gain in event rates can be obtained. However, more abundant processes such as $e^+e^- \rightarrow W^+W^-$ will obscure the signal unless the calorimeter is able to distinguish efficiently between hadronic decay of W and Z bosons.

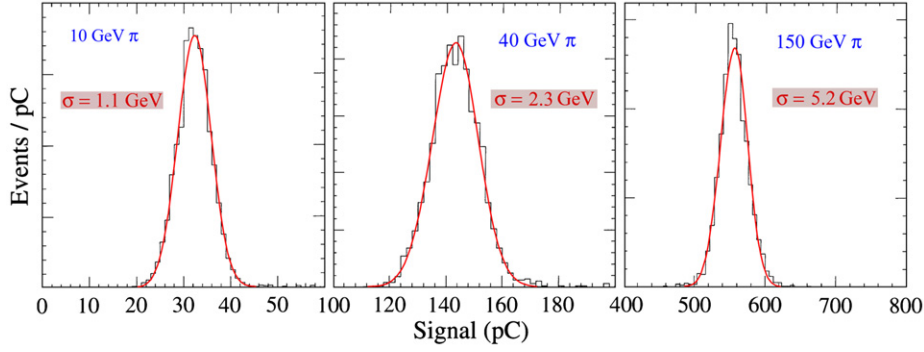


Fig. 20. Signal distributions for pions of 10, 40 and 150 GeV measured with the compensating Pb/plastic-scintillator SPACAL calorimeter [46].

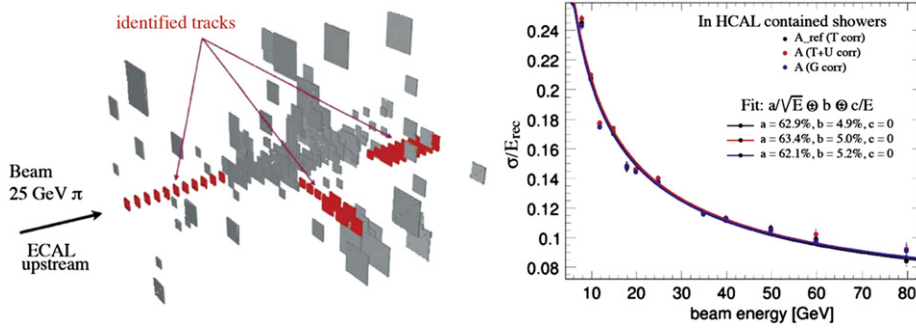


Fig. 21. Event display of a hadron shower in the CALICE calorimeter with identified track segments used for *in situ* mip calibration (left). Hadron energy resolution of the CALICE calorimeter obtained with mip calibration from the same and from a different test beam site, transported with *in situ* methods (right) [51].

the crucial hadronic W/Z separation has to be performed, the measured resolution is about 9%, *i.e.* more than a factor of two larger than needed.

As indicated in Section 4, calibration is a crucial task in a calorimeter system of this type. The mip calibration used for obtaining the results from Fig. 21 is a good starting point. However, the real issue is of course how to translate these data into particle, energy and position dependent numbers needed for determining the energy of showers developing in this structure. Given the complications described in Section 4.2, this will be a daunting task.

But *even if* this was successfully accomplished, one would still be faced with an even more challenging problem, namely how to avoid double counting, *i.e.* how to eliminate from the measured calorimetric energy deposit pattern the contributions from charged hadrons, whose momenta have been measured by the tracking system. There is no such thing as a “typical hadronic shower profile” that could be used for this purpose. This may be concluded from detailed measurements of the energy deposit profiles in a finely segmented lead/iron/plastic-scintillator calorimeter [13]. Fig. 22 shows the longitudinal profiles of 12 randomly selected events. The peaks in these profiles, which characterize the large event-to-event differences, are caused by em shower components. The figure demonstrates that such components are abundantly produced beyond the first nuclear interaction length, *i.e.* in the hadronic section of typical calorimeter systems. This feature is also the origin of calibration problems in segmented non-compensating calorimeters (see Section 4). Even more problematic for PFA purposes are the fluctuations in the plane perpendicular to the shower axis. These are similarly diverse. It is possible that a very fine calorimeter segmentation could help identifying the precise energy deposit patterns of individual showers developed by the charged jet fragments. However, this has yet to be proven in practice.

One of the concept ILC detectors that plan to use Particle Flow Analysis (GLD, one of the four concept detectors proposed for the ILC) does not rely entirely on the advocated PFA merits, but has chosen a compensating lead/plastic-scintillator hadronic calorimeter section. Measurements of hadronic showers developing in prototypes of this detector gave a resolution of ~ 4.5 GeV in the most relevant 80–90 GeV region [52], in good agreement with earlier measurements for a similar structure [47].

7.2. Dual-readout calorimetry

A completely different approach is followed by the DREAM Collaboration, which tries to meet the mentioned performance requirements by developing a calorimeter that can measure the jet energy sufficiently precisely by itself, *i.e.* without momentum information from the tracking system. Since the resolution is determined by fluctuations, eliminating or reducing the (effects of the) dominant fluctuations is the key to improving it.

In non-compensating calorimeters, the hadronic energy resolution is dominated by fluctuations in f_{em} . The mentioned effects of non-compensation on resolution, linearity and line shape, as well as the associated calibration problems are absent in compensating calorimeters ($e/h = 1.0$). Compensation can be achieved in sampling calorimeters with high- Z absorber material and hydrogenous active material. It requires a very specific sampling fraction, so that the response to shower neutrons is boosted by the precise factor needed to equalize e and h . For example, in Pb/scintillating-plastic structures, this sampling fraction is $\sim 2\%$ for showers [46,53,54]. This small sampling fraction sets a lower limit on the contribution of sampling fluctuations, while the need to efficiently detect MeV-type neutrons requires signal integration over a relatively large volume during at least 30 ns. Yet, calorimeters of this type currently hold the world record for hadronic energy resolution ($\sigma/E \sim 30\%/\sqrt{E}$ [46]).

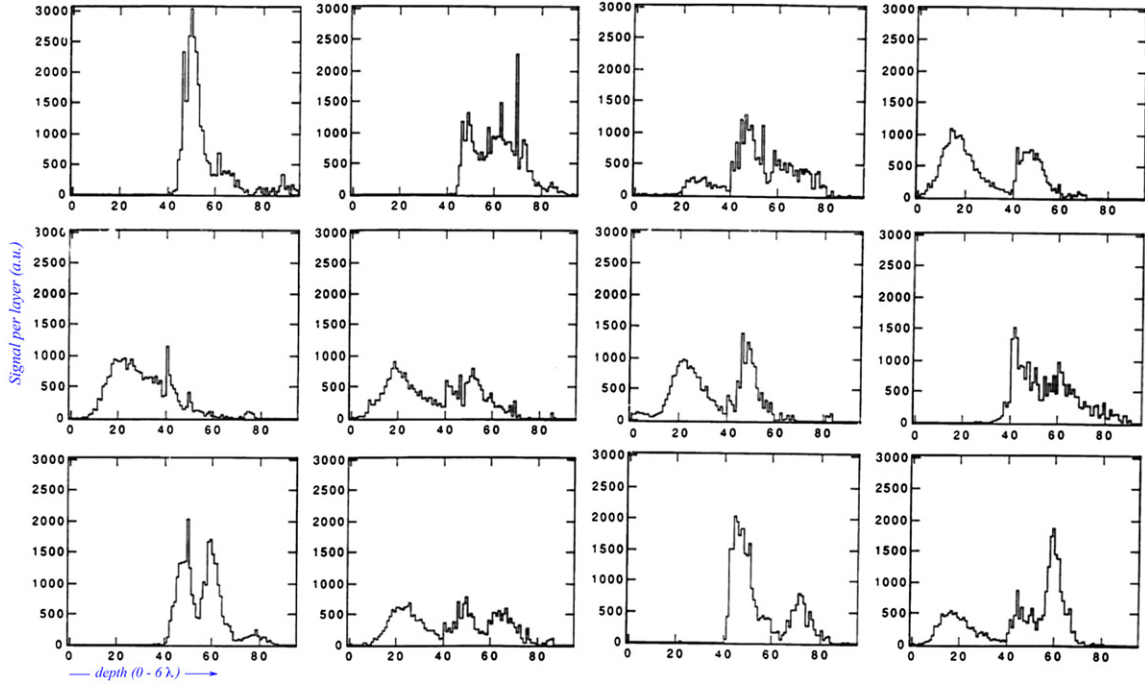


Fig. 22. Longitudinal energy deposit profiles for 270 GeV π^- showers in a lead/iron/plastic-scintillator calorimeter [13]. Shown are the longitudinal profiles for 12 randomly chosen events. For each event, the horizontal scale spans a total depth of six nuclear interaction lengths.

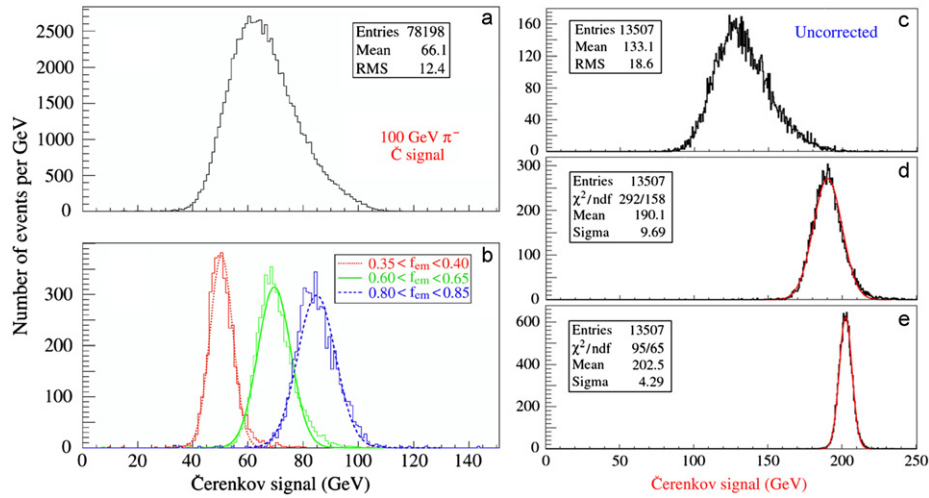


Fig. 23. Cherenkov signal distribution for 100 GeV π^- (a) and distributions for subsamples of events selected on the basis of the measured f_{em} value (b). Signal distributions for high-multiplicity 200 GeV “jets” in the DREAM calorimeter before (c) and after (d) corrections as described in the text were applied. In diagram (e), energy constraints were used, which eliminated the effects of lateral shower leakage fluctuations that dominate the resolution in (d).

The dual-readout approach aims to achieve the advantages of compensation without these disadvantages. The energy carried by the non-em shower component is mostly deposited by non-relativistic shower particles (protons), and therefore does not contribute to the signals of a Cherenkov calorimeter. By measuring simultaneously dE/dx and the Cherenkov light generated in the shower absorption process, one can determine f_{em} event by event and thus eliminate (the effects of) its fluctuations. The correct hadron energy can be determined from a combination of both signals.

This principle was first experimentally demonstrated by the DREAM Collaboration [55], with a Cu/fiber calorimeter. Scintillating fibers measured dE/dx , quartz fibers the Cherenkov light. The response ratio of these two signals, Q from clear and S from

scintillating fibers, is related to f_{em} as

$$\frac{Q}{S} = \frac{f_{em} + 0.21(1-f_{em})}{f_{em} + 0.77(1-f_{em})} \quad (5)$$

where 0.21 and 0.77 represent the h/e ratios of the Cherenkov and scintillator calorimeter structures, respectively. The hadron energy can be derived directly from the two signals:

$$E = \frac{\chi \times (S-Q)}{\chi-1}, \quad \text{with } \chi = \frac{[1-(h/e)_Q]}{[1-(h/e)_S]} = 3.43 \quad (6)$$

The merits of this method are illustrated in Fig. 23, which shows that the energy resolution improved, the signal distribution became much more Gaussian and, most importantly, the

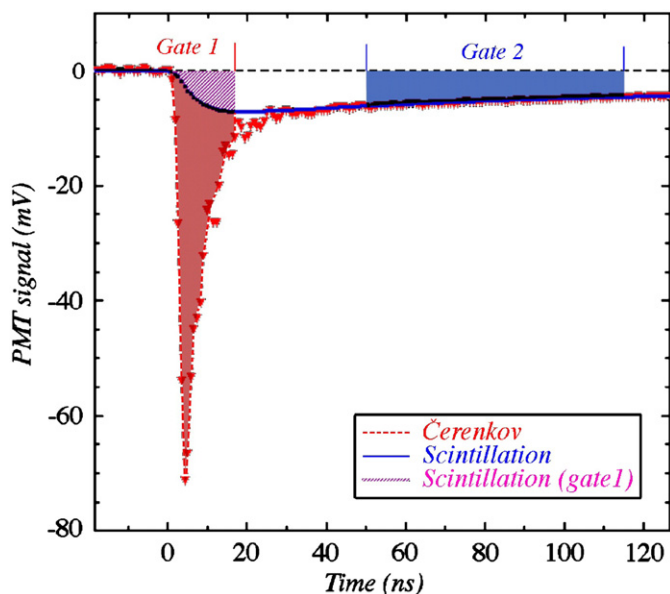


Fig. 24. The time structure of a typical shower signal measured in the BGO calorimeter equipped with a UV filter. These signals were measured with a sampling oscilloscope, which took a sample every 0.8 ns. The signals were used to measure the relative contributions of scintillation light (gate 2) and Cherenkov light (gate 1) [58].

hadronic energy was correctly reproduced in this way. This was true both for single pions and for multiparticle “jets.”

It was shown that similar results can also be obtained with high- Z crystal calorimeters (PbWO_4 , BGO), whose signals can be separated into scintillation and Cherenkov components [56–58]. This was achieved by making use of differences between the time structure and the photon spectra of both signal components.

Fig. 24 shows the time structure of BGO signals recorded with a UV filter. The “prompt” component observed in the ultraviolet signal is due to Cherenkov light. A small fraction of the scintillation light also passes through the UV filter, and is responsible for the tail in the time structure. This offers the possibility to obtain all needed information from that one signal. An external trigger opens two gates: one narrow (16 ns) gate covers the prompt component, the second gate (delayed by 30 ns and 65 ns wide) only contains scintillation light. The latter signal can also be used to determine the contribution of scintillation to the light collected in the narrow gate. In this way, the Cherenkov/scintillation ratio can be measured event-by-event on the basis of one signal only.

Detailed measurements of the time structure of the signals also make it possible to clear another important hurdle toward ultimate performance of hadron calorimeters, i.e. fluctuations in the energy fraction used to break up atomic nuclei.⁶ It has been demonstrated that the kinetic energy carried by the neutrons produced in the shower development process is correlated to this invisible energy loss [2]. Efficient neutron detection, a key ingredient for compensating calorimeters, not only brings e/h to 1.0, but also greatly reduces the contribution of fluctuations in invisible energy to the hadronic energy resolution. It has been demonstrated that this reduces the ultimate limit on this resolution to $\sim 13\%/\sqrt{E}$ [60], in compensating lead/plastic-scintillator calorimeters. This would translate into mass resolutions of $\sim 1.5\%$ for hadronically decaying W and Z bosons.

⁶ The elimination of fluctuations in f_{em} takes care of the effects of the average contribution of invisible energy. However, for a given value of f_{em} , the invisible energy fluctuates around this average.

Fig. 25 shows the average time structure of Cherenkov and scintillator signals measured for 100 GeV π^+ showers developing in the DREAM fiber calorimeter. The scintillator signals exhibit an exponential tail with a time constant of ~ 20 ns. This tail has all the characteristics expected of a (nonrelativistic) neutron signal and is thus absent in the time structure of the Cherenkov signals. Event-by-event analysis of the contribution of neutrons to the calorimeter signals showed that this contribution is anti-correlated to f_{em} , and makes it possible to further improve the energy resolution beyond the levels made possible by the dual-readout method [61].

7.3. Challenges

Many years of experience have shown that detectors based on light as the source of experimental information have their own characteristic problems. Among these, we mention the effects of light attenuation, short-term instabilities arising from temperature and other environmental effects, and long-term effects of radiation damage and other aging phenomena. Perhaps the most daunting challenges should be expected from light attenuation. The scale for fluctuations in hadronic shower development is set by the nuclear interaction length, typically ~ 20 cm in realistic detector structures. A typical characteristic of a dual-readout calorimeter is its longitudinally unsegmented structure, chosen deliberately to avoid the problems discussed in Section 4. If one wants to limit the effects of spatial shower fluctuations on the signals in such an unsegmented calorimeter to 1%, then the light attenuation length of the readout elements thus has to be ~ 20 m.⁷ This requirement will be extremely hard to achieve with active media other than optical fibers. On the other hand, it may be very hard to make a 4π detector structure with longitudinal optical fibers.

A second set of problems for light-based calorimeters arises from the need to operate in a magnetic field. Not only does this field affect the light production characteristics of some media, it also limits the choice of light detectors. New types of light detectors developed to deal with these problems (HPD, APD, SiPM) exhibit encouraging, but by no means ideal characteristics.

8. Non-accelerator applications of hadron calorimetry

All calorimeters discussed in the previous sections were man-made. In this section, we look into efforts to use our natural environment as a calorimeter. The driving force behind these efforts is the opportunity to create a very large instrument in this way. Typical detector volumes are measured in units of km^3 , i.e. at least four orders of magnitude larger than SuperKamiokande [63], which has one of the largest instrumented volumes of any man-made calorimeter. Such large volumes are needed to achieve the scientific goals of the experiments, which usually focus on the study of very rare natural phenomena. Examples of such phenomena include the absorption of extremely high-energy protons, α s or heavier atomic nuclei of extraterrestrial origin in the Earth's atmosphere and interactions of extra-galactic neutrinos in the Earth itself.

Almost all natural calorimeters are based on light as the source of experimental information. In one noteworthy exception, radio signals are exploited. Usually, the Cherenkov mechanism is the source of the signals, especially in detectors where sea water or

⁷ This number applies to single hadrons. The requirements are much less stringent for the detection of jets, since the depth fluctuations in light production decrease considerably for a number of particles that simultaneously develop showers in the same structure [62,55].

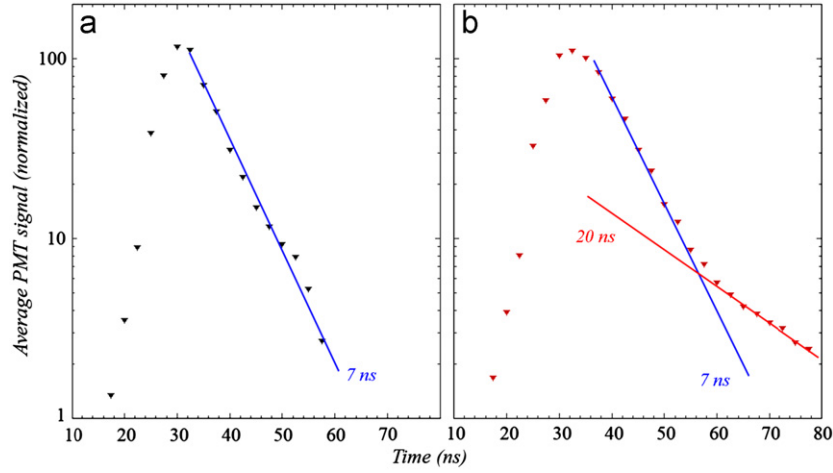


Fig. 25. The average time structure of the Cherenkov (a) and scintillator (b) signals measured for 100 GeV π^+ showers in a tower located on the shower axis. The shown PMT signals have been inverted to positive for convenience. The lines represent exponential fits to (parts of) the trailing edge of the signal shapes [59] (see text for details).

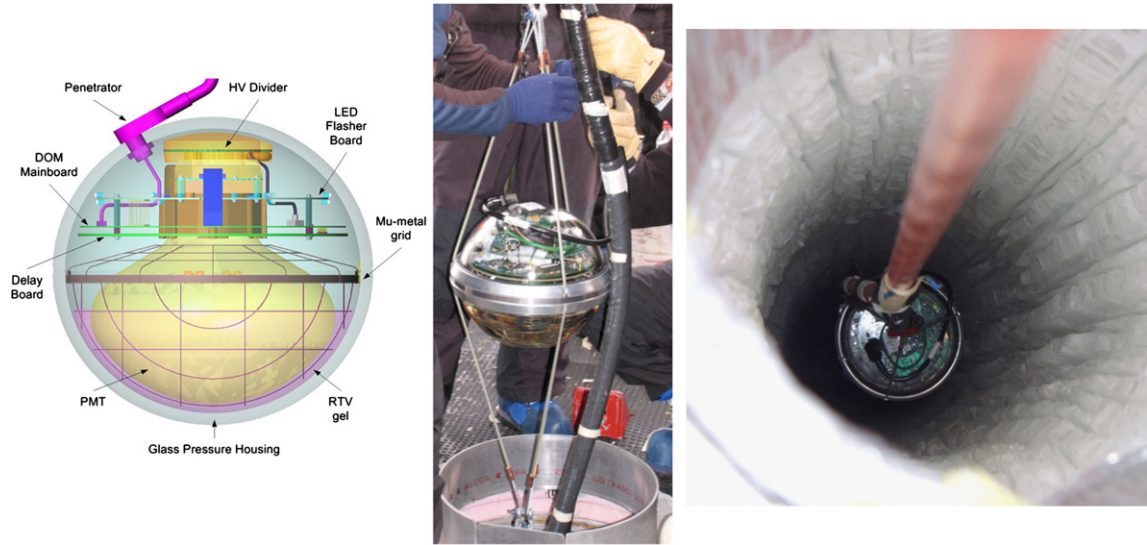


Fig. 26. One of the Digital Optical Modules used in the IceCube experiment. Shown are a schematic drawing of this module (left), the real thing assembled (center) and being lowered to its final position in the ice (right).

Arctic ice serve as the absorber medium. Cherenkov light is usually also an important source of experimental information in detectors using the Earth's atmosphere as a calorimeter. In some experiments of the latter type, scintillation light is used as well.

The technique to measure the Cherenkov light produced by extremely high-energy neutrinos of cosmic origin in water was pioneered in Lake Baikal (Siberia) by a consortium of Russian and German scientists [64]. A telescope consisting of a lattice of 200 large PMTs spread over a large open volume at a depth of ~ 1 km looks for upward traveling muons produced in neutrino interactions in water in the vicinity of the detector. Since the angle between the parent neutrino and the muon produced in the interaction is very small, high-resolution astronomy is in principle possible. The direction of the particle can be inferred from the measured arrival times and amplitudes of the Cherenkov photons observed in the various PMTs. The same technique is applied, on a much larger scale, in the Antarctic ice near the Amundsen-Scott South Pole station. The IceCube experiment [65,66] has currently installed 4740 PMTs covering a volume of $\sim 1 \text{ km}^3$ at a depth ranging from 1450 to 2450 m below the surface (Fig. 26).

Another structure of similar dimensions is planned for installation somewhere in the Mediterranean. Exploratory work in that

context has been carried out by the ANTARES [67], NEMO [68] and NESTOR [69] Collaborations. Some advantages of ice over water in a lake or sea include the absence of light emitting organisms and underwater currents that may jeopardize the integrity of the detector structure. On the other hand, light scattering by air bubbles trapped in ice may limit the possibilities to reconstruct the direction of the incoming particles.

The operation of detectors of this type is of course very different from those in accelerator laboratories. Whereas muons are usually referred to as “minimum ionizing particles” (mips) in accelerator based experiments, IceCube uses the non-mip nature of these particles to calibrate the energy scale of their detector, exploiting the fact that the specific energy loss (dE/dx) depends logarithmically on the muon energy in the region of interest (TeV–EeV). The angular resolution of their instrument ($< 0.5^\circ$) is measured using the shadow of the Moon, which measurably affects the rate of down-going atmospheric muons. With this kind of resolution one might hope to detect point sources of extraterrestrial neutrinos.

The Antarctic ice cap is also the source of signals for the ANITA experiment [70], which aims to detect the radio component of the coherent Cherenkov signals produced as a result of the charge



Fig. 27. One of the Cherenkov telescopes used in the HEGRA experiment at La Palma. Photo courtesy K. Bernlohr.

asymmetry in high-energy em showers, the so-called Askaryan effect [71]. This mechanism may also be exploited in other media that are transparent to such radio signals, for example large rock salt formations [72].

Experiments using the Earth's atmosphere as a calorimeter are primarily looking for extensive air showers caused by very-high-energy charged cosmic particles. At sea level, the atmosphere represents an absorber with a total thickness of $\sim 11\lambda_{\text{int}}$, or $\sim 28X_0$, enough to absorb even the highest energy particles to a very large extent. The Cherenkov light produced in the absorption process is relatively easy to detect, provided that it is emitted in the direction of the telescope that is looking for it (Fig. 27). Because of the very small refraction index of air, the Cherenkov angle is very small and only energetic shower particles produced in the early stages of the shower development emit Cherenkov light. As a result, this light is highly collimated, a shower starting at the typical altitude of 10 km produces a light cone at ground level with a radius of only ~ 100 m. Therefore, modern experiments looking for hadronic showers complement the Cherenkov telescopes with additional detectors, looking for (isotropically emitted) fluorescent light (produced by transitions in molecular nitrogen and in N_2^+ ions), for muons from decaying shower particles (π, K), and/or shower particles themselves. Examples of such experiments include AUGER [73] and KASCADE-Grande [74] (hadronic showers) and VERITAS [75] and HESS [76] (em showers). The angular resolutions of these experiments are even better than those obtained with IceCube. Apart from the shadowing effect of the Moon [77], one can also use the signals from some known point sources of γ rays for this purpose. The signals from the strongest of these sources, the Crab nebula, is also a valuable tool for the energy calibration. Variations of the order of 20% between the different experiments that use this technique [78] are indicative for the relative uncertainty in the energy scale. More information about this exciting field and the role played by hadron calorimeters in advancing it can be found in Ref. [79].

9. Summary

We would like to finish this review with some concluding remarks that we expect will serve the developers of future detectors, as well as users of present ones.

- If a dedicated hadron calorimeter is equipped with a separate em section that has the purpose to measure em showers with better

precision, then the hadronic energy resolution of the combined system is worse than that of the hadronic section alone, especially at high energies. In cases like ATLAS and CMS, the performance of the combined calorimeters is what matters.

- Longitudinal segmentation of a calorimeter system greatly complicates the calibration of the calorimeter system, and may in fact make a correct calibration impossible in practice.
- Positioning readout elements inside the absorber structure (between the em and hadronic sections, for example) should be avoided because this introduces spurious signals due to interactions in the photosensors. The hadronic shower maximum takes place roughly after one interaction length, comparable with the depth of typical em sections.
- Energy resolution is determined by event-to-event fluctuations, not by average values. This means that attempts to improve the energy resolution of a longitudinally segmented calorimeter by applying different global weight factors to signals from different segments are not meaningful. For the same reason, the presumed advantage of Particle Flow Analysis is doubtful. If only the charged jet fragments were measured, the jet energy resolution would not be better than $\sim 20\%$, at any energy [80].
- Quoting hadronic energy resolutions in terms of $\kappa\%/\sqrt{E}$ is typically not very meaningful. Especially when the instrument is intended for measurements at high energies, its resolution tends to be dominated by deviations from $E^{-1/2}$ scaling. In addition, statements about energy resolution are only meaningful if they include the effects of non-linearity, which apply to almost all calorimeter systems currently in use or planned. Signal non-linearity introduces additional uncertainties in the mean value of the response function for jets, which have to be taken into account if one wants to address the precision with which the energy of individual jets can be measured.
- Monte Carlo simulations have been improving both in physics content and in precision over the last decade, but the ultimate truth lies in experimental data, often obtained in well executed beam tests.

References

- [1] R. Brown, D. Cockerill, Nuclear Instrumentation and Methods in Physics Research Section A, doi:10.1016/j.nima.2011.03.017, this issue.
- [2] R. Wigmans, Calorimetry: Energy measurement in particle physics, in: International Series of Monographs on Physics, vol. 107, 2000, pp. 1–726.
- [3] D. Green, Cambridge Monographs on Particle Physics, Nuclear Physics and Cosmology 12 (2000) 1.
- [4] C. Grupen, B. Schwartz, Particle Detectors, Cambridge University Press, Cambridge, UK, 2008, p. 651.
- [5] C. Leroy, P.-G. Rancoita, Principles Of Radiation Interaction in Matter and Detection, ISBN-13-9789812389091.
- [6] C.W. Fabjan, F. Gianotti, Reviews of Modern Physics 75 (2003) 1243. doi:10.1103/RevModPhys.75.1243.
- [7] C. Amsler, et al., Physics Letters B 667 (2008) 1. doi:10.1016/j.physletb.2008.07.018.
- [8] M.G. Albrow, et al., Nuclear Instrumentation and Methods in Physics Research Section A 431 (1999) 104. doi:10.1016/S0168-9002(99)00250-8.
- [9] D. Acosta, et al., Nuclear Instrumentation and Methods in Physics Research Section A 302 (1991) 36. doi:10.1016/0168-9002(91)90489-D.
- [10] H. Abramowicz, et al., Nuclear Instrumentation and Methods in Physics Research Section A 180 (1981) 429. doi:10.1016/0029-554X(81)90083-5.
- [11] P. Adragna, et al., Nuclear Instrumentation and Methods in Physics Research Section A 606 (2009) 362. doi:10.1016/j.nima.2009.04.009.
- [12] P. Adragna, et al., Nuclear Instrumentation and Methods in Physics Research Section A 615 (2010) 158. doi:10.1016/j.nima.2010.01.037.
- [13] D. Green, Selected topics in sampling calorimetry, Prepared for 4th International Conference on Calorimetry in High-energy Physics, La Biodola, Italy, 19–25 September 1993.
- [14] M.G. Albrow, et al., Nuclear Instrumentation and Methods in Physics Research Section A 487 (2002) 381. doi:10.1016/S0168-9002(01)02190-8.
- [15] R. Wigmans, AIP Conference Proceeding 867 (2006) 90. doi:10.1063/1.2396942.
- [16] TESLA Technical Design Report, Report DESY 2001-011.

- [17] C. Adloff, et al., CALICE Report to the Calorimeter R&D Review Panel, arxiv:0707.1245.
- [18] D. Acosta, et al., Nuclear Instrumentation and Methods in Physics Research Section A 316 (1992) 184. doi:10.1016/0168-9002(92)90901-F.
- [19] N. Akchurin, et al., Nuclear Instrumentation and Methods in Physics Research Section A 399 (1997) 202. doi:10.1016/S0168-9002(97)00789-4.
- [20] T. Gabriel, et al., Nuclear Instrumentation and Methods in Physics Research Section A 338 (1994) 336.
- [21] N. Akchurin, et al., Nuclear Instrumentation and Methods in Physics Research Section A 408 (1998) 380. doi:10.1016/S0168-9002(98)00021-7.
- [22] J.B. Birks, The Theory and practice of scintillation counting, in: International series of Monographs on Electronics and Instrumentation, vol. 27, Macmillan, New York.
- [23] I. Galaktionov, et al., Nuclear Instrumentation and Methods in Physics Research Section A 251 (1986) 258. doi:10.1016/0168-9002(86)90790-4.
- [24] S. Cihangir, F. Marchetto, P. McIntyre, T. Meyer, R. Webb, Nuclear Instrumentation and Methods in Physics Research Section A 267 (1988) 249. doi:10.1016/0168-9002(88)90472-X.
- [25] S. Cihangir, et al., IEEE Transactions on Nuclear Science NS-36 (1989) 347. doi:10.1109/23.34462.
- [26] D.E. Groom, Nuclear Instruments and Methods in Physics Research Section A: Accelerators, Spectrometers, Detectors and Associated Equipment 572 (2) (2007) 633. doi:10.1016/j.nima.2006.11.070.
- [27] N. Akchurin, et al., The response of CMS combined calorimeters to single hadrons, electrons and muons, CERN-CMS-NOTE-2007-012.
- [28] O. Ganel, R. Wigmans, Nuclear Instrumentation and Methods in Physics Research Section A 409 (1998) 621. doi:10.1016/S0168-9002(97)01337-5.
- [29] F. Cervelli, et al., Nuclear Instrumentation and Methods in Physics Research Section A 490 (2002) 132. doi:10.1016/S0168-9002(02)00915-4.
- [30] T. Akesson, et al., Nuclear Instrumentation and Methods in Physics Research Section A 262 (1987) 243. doi:10.1016/0168-9002(87)90862-X.
- [31] R. Wigmans, M.T. Zeyrek, Nuclear Instrumentation and Methods in Physics Research Section A 485 (2002) 385. doi:10.1016/S0168-9002(01)02141-6.
- [32] M. Aharrouché, et al., Nuclear Instrumentation and Methods in Physics Research Section A 568 (2006) 601. doi:10.1016/j.nima.2006.07.053 arxiv: physics/0608012.
- [33] ATLAS-Collaboration, ATLAS Tile calorimeter: Technical Design Report, CERN-LHCC-96-42, 1996, p. 347.
- [34] E. Abat, et al., Nuclear Instrumentation and Methods in Physics Research Section A 607 (2009) 372. doi:10.1016/j.nima.2009.05.158.
- [35] E. Abat, et al., Nuclear Instrumentation and Methods in Physics Research Section A 621 (2010) 134. doi:10.1016/j.nima.2010.04.054.
- [36] S. Abdullin, et al., European Physical Journal C 60 (2009) 359. doi:10.1140/epjc/s10052-009-0959-5.
- [37] S. Abdullin, et al., European Physical Journal C 55 (2008) 159. doi:10.1140/epjc/s10052-008-0573-y.
- [38] S. Abdullin, et al., European Physical Journal C 57 (2008) 653. doi:10.1140/epjc/s10052-008-0756-6.
- [39] A. Andresen, et al., Nuclear Instrumentation and Methods in Physics Research Section A 290 (1990) 95. doi:10.1016/0168-9002(90)90347-9.
- [40] S. Agostinelli, et al., Nuclear Instrumentation and Methods in Physics Research Section A 506 (2003) 250. doi:10.1016/S0168-9002(03)01368-8.
- [41] A. Ribon, et al., Status of GEANT4 Hadronic Physics for the Simulation of LHC Experiments at the Start of LHC Physics Program, CERN-LCGAPP-2010-02.
- [42] P.V. Degtyarenko, M.V. Kosov, H.P. Wellisch, European Physical Journal A 8 (2000) 217. doi:10.1007/s100500070108.
- [43] P.V. Degtyarenko, M.V. Kossov, H.P. Wellisch, European Physical Journal A 9 (2000) 411. doi:10.1007/s100500070025.
- [44] P.V. Degtyarenko, M.V. Kossov, H.P. Wellisch, European Physical Journal A 9 (2000) 421. doi:10.1007/s100500070026.
- [45] K. Seidel, et al., Particle Showers in a Highly Granular Hadron Calorimeter arxiv:1004.2587v1.
- [46] D. Acosta, et al., Nuclear Instrumentation and Methods in Physics Research Section A 308 (1991) 481. doi:10.1016/0168-9002(91)90062-U.
- [47] U. Behrens, et al., Nuclear Instrumentation and Methods in Physics Research Section A 289 (1990) 115. doi:10.1016/0168-9002(90)90253-3.
- [48] D. Buskulic, et al., Nuclear Instrumentation and Methods in Physics Research Section A 360 (1995) 481. doi:10.1016/0168-9002(95)00138-7.
- [49] <http://physics.uoregon.edu/~lc/wwwstudy/concepts/>.
- [50] M. Albrow, R. Raja, (Eds.), Hadronic shower simulation, in: Proceedings, Workshop, Batavia, USA, September 6–8, 2006, Prepared for Hadronic Shower Simulations Workshop, Batavia, Illinois, 6–8 September 2006.
- [51] Report to the DESY PRC arxiv:1003.1394v1.
- [52] S. Uozumi, et al., Nuclear Instrumentation and Methods in Physics Research Section A 487 (2002) 291. doi:10.1016/S0168-9002(01)00891-9.
- [53] E. Bernardi, et al., Nuclear Instrumentation and Methods in Physics Research Section A 262 (1987) 229. doi:10.1016/0168-9002(87)90861-8.
- [54] T. Suzuki, et al., Nuclear Instrumentation and Methods in Physics Research Section A 432 (1999) 48. doi:10.1016/S0168-9002(99)00394-0.
- [55] N. Akchurin, et al., Nuclear Instrumentation and Methods in Physics Research Section A 537 (2005) 537. doi:10.1016/j.nima.2004.07.285.
- [56] N. Akchurin, et al., Nuclear Instrumentation and Methods in Physics Research Section A 595 (2008) 359. doi:10.1016/j.nima.2008.07.136.
- [57] N. Akchurin, et al., Nuclear Instrumentation and Methods in Physics Research Section A 584 (2008) 273. doi:10.1016/j.nima.2007.09.035 arxiv:0707.4021.
- [58] N. Akchurin, et al., Nuclear Instrumentation and Methods in Physics Research Section A 598 (2009) 710. doi:10.1016/j.nima.2008.10.010.
- [59] N. Akchurin, et al., Nuclear Instrumentation and Methods in Physics Research Section A 581 (2007) 643. doi:10.1016/j.nima.2007.08.049 arxiv:0707.4019.
- [60] G. Drews, et al., Nuclear Instrumentation and Methods in Physics Research Section A 290 (1990) 335. doi:10.1016/0168-9002(90)90549-L.
- [61] N. Akchurin, et al., Nuclear Instrumentation and Methods in Physics Research Section A 598 (2009) 422. doi:10.1016/j.nima.2008.09.045.
- [62] D. Acosta, et al., Nuclear Instrumentation and Methods in Physics Research Section A 309 (1991) 143. doi:10.1016/0168-9002(91)90096-9.
- [63] S. Fukuda, et al., Nuclear Instrumentation and Methods in Physics Research Section A 501 (2003) 418. doi:10.1016/S0168-9002(03)00425-X.
- [64] <http://baikalweb.jinr.ru/>.
- [65] S.R. Klein, IEEE Transactions on Nuclear Science NS-56 (2009) 1141. doi:10.1109/TNS.2009.2015300 arxiv:0807.0034.
- [66] F. Halzen, S.R. Klein, Review of Scientific Instruments 81 (2010) 081101. doi:10.1063/1.3480478 arxiv:1007.1247.
- [67] <http://antares.in2p3.fr/>.
- [68] <http://nemoweb.lns.infn.it/>.
- [69] <http://www.nestor.noa.gr/>.
- [70] <http://www.phys.hawaii.edu/anita/web/index.html/>.
- [71] G. Askaryan, Soviet Physics JETP 14 (1961) 441.
- [72] P. Gorham, et al., Nuclear Instrumentation and Methods in Physics Research Section A 490 (2002) 476. doi:10.1016/S0168-9002(02)01077-X arxiv:hep-ex/0108027.
- [73] <http://www.auger.org/>.
- [74] <http://www-ik.fzk.de/KASCADE/>.
- [75] <http://veritas.sao.arizona.edu/>.
- [76] <http://www.mpi-hd.mpg.de/hfm/HESS/>.
- [77] C.M. Hoffman, C. Sennis, P. Fleury, M. Punch, Review in Modern Physics 71 (1999) 897. doi:10.1103/RevModPhys.71.897.
- [78] F.A. Aharonian, et al., Astrophysics Journal 539 (2000) 317. doi:10.1086/309225 arxiv:astro-ph/0003182.
- [79] R. Clay, B.R. Dawson, Cosmic Bullets: High Energy Particles in Astrophysics, Allen and Unwin, St Leonards, N.S.W., 1997.
- [80] O. Lobban, A. Sriharan, R. Wigmans, Nuclear Instrumentation and Methods in Physics Research Section A 495 (2002) 107. doi:10.1016/S0168-9002(02)01615-7.